Chemical Science

ROYAL SOCIETY OF CHEMISTRY

REVIEW

View Article Online
View Journal | View Issue

Cite this: *Chem. Sci.*, 2026, **17**, 3449

Mechanistic insights and catalyst design for the selective hydrogenolysis of cellulose to C_2–C_3 alcohols

Yuandong Cui,[a] Dandan Wang,[a] Haoxi Ben,[a] Xiong Su, *[b] Xiaoli Yang*[a] and Yanqiang Huang [b]

Catalytic hydrogenolysis of cellulose into low-carbon alcohols offers a promising route toward sustainable chemical manufacture and carbon-neutral energy systems. Recent advances in aqueous-phase catalysis have progressively clarified the reaction network encompassing cellulose depolymerization, glucose isomerization, retro-aldol C–C scission, and the hydrogenation of key carbonyl intermediates. This review integrates these mechanistic insights with catalyst and process design, highlighting how noble-metal and non-noble bifunctional systems leverage acid–metal cooperation, redox flexibility, and spatial confinement to orchestrate glycosidic, C–O, and C–C bond activation with increasing precision. Kinetic and engineering studies further reveal how reactor configuration, operating conditions, and feedstock pretreatment shape conversion efficiency and carbon utilization in both batch and continuous modes. Emerging opportunities, including single-atom catalysts that maximize atom efficiency and enable precise site control, defect-engineered oxides, machine-learning-assisted discovery for accelerated catalyst optimization, and integrated reaction-separation platforms, hold considerable promise for enabling cost-effective, scalable, and recyclable catalytic systems. Together, these advances establish a coherent framework linking fundamental chemistry with reactor-level engineering, laying the groundwork for practical one-step aqueous-phase routes to bio-derived low-carbon alcohols.

Received 8th December 2025
Accepted 21st January 2026

DOI: 10.1039/d5sc09595f

rsc.li/chemical-science

1 Introduction

The global energy system is undergoing an unprecedented transition driven by the pursuit of carbon neutrality and sustainable growth.[1] Decades of dependence on fossil fuels have powered industrialization but also intensified greenhouse-gas emissions, resource depletion, and environmental degradation.[2–4] These intertwined challenges have spurred the search for renewable carbon resources capable of supporting a circular and low-carbon chemical economy. Among them, biomass stands out as the only renewable reservoir of organic carbon,[5] offering an essential foundation for the production of green fuels and value-added chemicals (Fig. 1). It is projected that the global biomass market size will grow from USD 79.26 billion in 2025 to USD 157.38 billion in 2035.[6] However, the utilization rate of cellulosic resources available for industrial processes remains relatively low at present. The contradiction between such enormous resource potential and the currently limited industrial conversion efficiency highlights that the value-added utilization of biomass has become a pivotal pathway to achieve energy security and environmental sustainability.[7,8]

Cellulose, the most abundant polysaccharide in nature, is a major structural component of lignocellulosic biomass derived from agricultural residues, woody materials, and non-food herbaceous plants. Composed of D-glucose units connected through β-1,4-glycosidic bonds, cellulose forms a rigid crystalline network that provides structural strength to biomass yet poses intrinsic challenges to its chemical transformation.[9–12] Unlike starch or sugar-based feedstocks, cellulose conversion avoids competition with food resources and thus enables large-

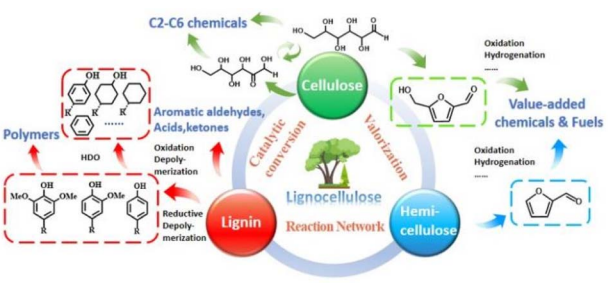

Fig. 1 Catalytic conversion network for value-added utilization of lignocellulosic biomass. Reproduced with permission.[5] Copyright 2023, the Royal Society of Chemistry.

[a]College of Textiles and Clothing, State Key Laboratory of Bio-Fibers and Eco-textiles, Qingdao University, Qingdao 266071, P. R. China. E-mail: xlyang@qdu.edu.cn
[b]State Key Laboratory of Catalysis, Dalian Institute of Chemical Physics, Chinese Academy of Sciences, Dalian 116023, P. R. China. E-mail: suxiong@dicp.ac.cn

scale deployment without disrupting the food-energy-environment nexus. Its selective transformation into low-carbon alcohols—such as ethanol (EtOH), ethylene glycol (EG), and 1,2-propylene glycol (1,2-PG)—represents a promising route to bridge renewable carbon with existing chemical and fuel infrastructures.[13–15] These polyfunctional alcohols serve as key intermediates for polymers, solvents, food and pharmaceutical products, and fine chemicals, with their global market scale continuously expanding.[16] Consequently, the direct catalytic conversion of abundant cellulose resources into these high-value chemicals holds significant strategic and economic importance.

Multiple strategies have been developed to convert cellulose into low-carbon alcohols, including biological fermentation,[17] acid hydrolysis coupled with fermentation,[18] and thermochemical processes such as gasification-synthesis.[19] Despite their maturity, biological routes suffer from low carbon efficiency, high enzyme cost, and complex pretreatment requirements,[17,20,21] while gasification demands high temperature, high pressure, and substantial capital investment.[22] In contrast, catalytic hydrogenolysis has emerged as a more direct and atom-efficient approach capable of simultaneously cleaving C–C and C–O bonds and hydrogenating intermediates under comparatively mild aqueous conditions.[23–25] This thermochemical pathway offers high atom economy, controllable selectivity, and potential scalability, making it a cornerstone technology for sustainable biomass valorization.

During the past two decades, significant progress has been made in elucidating and optimizing the aqueous-phase hydrogenolysis of cellulose. The development of bifunctional catalysts integrating metallic and acidic sites, such as W-, Ni-, Ru-, and Pt-based systems,[26–30] has markedly improved reaction efficiency and product selectivity. Mechanistic studies have further revealed that cellulose depolymerization, glucose isomerization, retro-aldol condensation (RAC), and hydrogenation occur through interconnected steps requiring precise spatial and electronic coordination between active sites.[31–34] In particular, the cooperative interplay between acid and metal centers, exemplified in catalysts such as Pt–WO_x, Ni–WO_x, and PdZn-zeolite frameworks, determines the dominant reaction pathway and selectivity toward EG, 1,2-PG, ethanol, or polyols. These mechanistic insights have inspired the design of new generations of spatially confined, electronically modulated catalysts featuring enzyme-like efficiency and stability under hydrothermal conditions.

In parallel, advances in reactor design and process intensification have bridged the gap between molecular reactivity and engineering scalability. The transition from batch to semi-continuous and continuous-flow systems has provided deeper kinetic understanding and improved control over intermediate concentration, hydrogen supply, and mass transport—key factors for achieving high selectivity and yield at scale.[31,33] Furthermore, optimized feedstock pretreatment and hybrid catalytic systems have extended the applicability of aqueous-phase hydrogenolysis from pure cellulose to raw lignocellulosic biomass, addressing issues associated with lignin, waxes, and mineral impurities.[34]

This review provides a comprehensive yet critical assessment of recent developments in the aqueous-phase catalytic hydrogenolysis of cellulose into low-carbon alcohols. Beginning with mechanistic insights that define the fundamental reaction network, it examines how these principles guide the rational design of catalytic systems—from noble and non-noble metals to tungsten-based multifunctional catalysts. Subsequent sections explore product-oriented reaction pathways and structure–selectivity relationships for ethanol, EG, 1,2-PG, and polyols, followed by a discussion of reactor engineering, feedstock utilization, and techno-economic considerations. The review concludes with emerging challenges and opportunities, emphasizing the integration of molecular catalysis, materials innovation, and process engineering as the foundation for scalable, sustainable biomass-to-alcohol conversion.

2 Mechanistic insights

Mechanistic understanding constitutes the cornerstone of rational catalyst design and process optimization in biomass conversion. In the case of cellulose hydrogenolysis, elucidating how macromolecular activation, C–C and C–O bond cleavage, and hydrogenation steps interconnect is essential for achieving selective transformation into low-carbon alcohols. The overall reaction does not proceed through a single step but rather a cascade of hydrolysis, isomerization, RAC, hydrogenation, and dehydration, each governed by distinct active sites and kinetic regimes. Over the past decade, research in this field has shifted from empirical catalyst screening toward an integrated, molecular-level comprehension of how catalyst structure and reaction environment jointly dictate product distribution. The following discussion traces this mechanistic evolution—from the organization of the overall reaction network and its elementary steps, through the kinetic and molecular evidence supporting these pathways, to the emerging understanding of how catalyst structure modulates C–C and C–O bond scission to control product selectivity.

2.1 Reaction framework

The crystalline microfibrils of cellulose are stabilized by dense intra- and intermolecular hydrogen bonding,[35] which endows them with exceptional rigidity and chemical resistance. These structural features originating from the β-(1,4)-linked D-glucopyranose framework pose formidable challenges for activation and depolymerization. Early attempts to transform cellulose into low-carbon alcohols, dating back to the 1930s,[36,37] were limited by poor substrate accessibility and minimal control over the complex reaction sequence, typically yielding <40% of target products.[37–39] A breakthrough occurred in 2008, when Zhang and co-workers achieved a 61% yield of EG from cellulose using a Ni–W_2C/AC catalyst.[40] This so-called "direct lignocellulose-to-ethylene glycol" (DLEG) strategy[41] demonstrated the feasibility of one-step catalytic hydrogenolysis, stimulating extensive mechanistic exploration into C–C/C–O bond cleavage and product selectivity.[42–44]

Cellulose hydrogenolysis proceeds through a sequence of interconnected elementary transformations that collectively govern product distribution. Conceptually, the process can be viewed as a tandem sequence integrating hydrolysis of β-1,4-glycosidic bonds with hydrogen-assisted deoxygenation reactions.[45] Hydrolysis generates glucose monomers, which subsequently undergo isomerization, RAC, hydrogenation, and dehydration to yield smaller oxygenates and polyols. Because these steps exhibit distinct kinetic and thermodynamic characteristics,[46–49] efficient conversion demands catalysts combining metal and acid functionalities in a finely tuned balance. Acid sites catalyze glycosidic-bond cleavage and sugar RAC or isomerization, whereas metal sites facilitate selective hydrogenation and C–C bond activation. Only when these functions operate synergistically can the network progress in a concerted manner, avoiding over-hydrogenation of intermediates or uncontrolled degradation—a dynamic equilibrium that ultimately shapes the selectivity landscape.[50,51]

Within this intricate network (Fig. 2), multiple pathways coexist for the generation of low-carbon alcohols. The primary EG pathway involves cellulose hydrolysis to glucose, followed by RAC of glucose into erythrose and glycolaldehyde, which is rapidly hydrogenated to EG. Under more reductive environments, EG can undergo further hydrogenative dehydration to ethanol, indicating a shared upstream chemistry in which EG and ethanol diverge primarily in the degree of reduction. In contrast, 1,2-PG originates from an alternative route—glucose isomerizes to fructose, which then undergoes RAC to form C_3 intermediates such as glyceraldehyde and dihydroxyacetone; these are subsequently hydrogenated to 1,2-PG. Because this route requires additional rearrangements and hydrogen-transfer steps, its overall carbon efficiency is typically lower than that of EG formation.

Besides RAC, alternative cleavage modes, such as *retro*-Claisen (RC) condensations, can contribute to EG formation by converting C_3 intermediates into glycolaldehyde under alkaline or bifunctional catalytic conditions.[52,53] Although this route enhances EG selectivity, it may compromise 1,2-PG yields. Excessive hydrogenation activity can further redirect intermediates toward hexitols such as sorbitol or mannitol. These polyols can undergo partial dehydrogenation to regenerate ketose species (*e.g.*, fructose), which re-enter the RAC cycle.[54–56] These forward and backward transformations underscore a dynamic interplay between hydrogenation and bond-scission reactions that governs overall product distribution. Excessive hydrogenation yields unreactive polyols, while insufficient reduction promotes over-fragmentation and carbon loss.

Mechanistic studies consistently demonstrate that selectivity toward EG or 1,2-PG is dictated by the relative kinetics of hydrogenation *versus* RAC. This kinetic balance is highly sensitive to the ratio and spatial proximity of metal and acid sites within the catalyst.[57,58] Metal-dominant catalysts accelerate hydrogenation but risk over-reduction, whereas acid-rich systems promote C–C cleavage but can induce dehydration and condensation side reactions.[59,60] Bifunctional catalysts with optimized metal–acid synergy, such as W-based oxides or Ru/Ni-supported systems, achieve concurrent activation and stabilization of intermediates, maximizing diol selectivity. The mechanistic principle of balanced bifunctionality thus provides the conceptual foundation for rational catalyst design, integrating hydrolysis, C–C scission, and hydrogenation within a unified catalytic cycle. These mechanistic hypotheses form the conceptual basis for the kinetic and molecular-level investigations discussed below.

Overall, the hydrogenolysis of cellulose can be rationalized through three recurring elementary motifs: (i) RAC of glucose-type intermediates yielding C_2–C_4 fragments (EG pathway); (ii) RAC of fructose-type intermediates generating C_3 species (1,2-PG pathway); and (iii) direct hydrogenation of erythrose-like intermediates producing polyols. These routes frequently operate simultaneously, and their relative importance is determined by the catalyst structure and reaction environment. Understanding and orchestrating these competing elementary steps is fundamental to developing highly selective hydrogenolysis systems for the sustainable production of low-carbon alcohols.

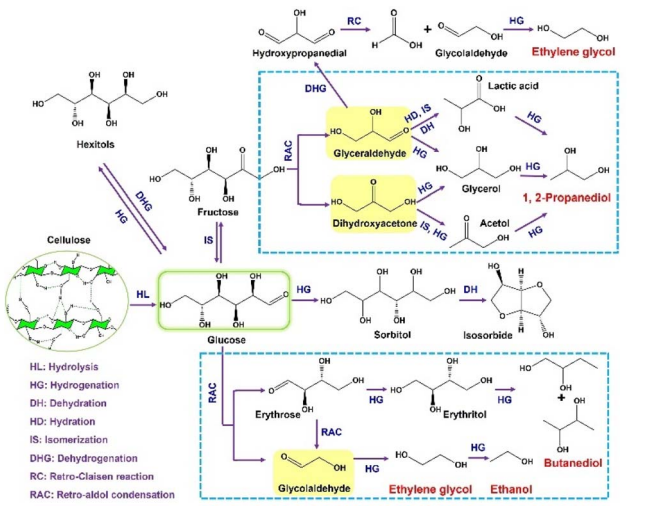

Fig. 2 Possible reaction pathways involved in catalytic conversion of cellulosic biomass to low-carbon alcohols.

2.2 Mechanistic and kinetic evidence

Mechanistic and kinetic investigations have provided the quantitative foundation for understanding the multistep cascade governing cellulose hydrogenolysis to low-carbon alcohols. As discussed above, the transformation involves sequential hydrolysis, RAC, and hydrogenation, accompanied by numerous parallel and competing reactions that jointly determine selectivity.[42] Over the past decade, this complex network has been systematically dissected through kinetic modeling, isotopic tracing, and reactor-scale analyses, revealing how intrinsic kinetics, surface adsorption, and process dynamics interconnect to shape EG and 1,2-PG yields.

The one-pot conversion of cellulose to EG follows a characteristic three-step sequence: hydrolysis of β-1,4-glycosidic bonds to release glucose; RAC of glucose to glycolaldehyde catalyzed by Lewis acid sites;[61] and hydrogenation of glycolaldehyde to EG

over metallic sites. However, this idealized sequence is complicated by the high reactivity of intermediates such as glucose, fructose, and glycolaldehyde, which can undergo isomerization, condensation, or over-hydrogenation.[48,49] Glucose may isomerize to fructose or hydrogenate to hexitols (*e.g.*, sorbitol, mannitol), competing with the RAC pathway. Fructose-derived C_3 intermediates—glyceraldehyde and dihydroxyacetone—yield 1,2-PG upon hydrogenation,[48–50] while reactive aldehydes like glycolaldehyde and glyceraldehyde condense to form higher oxygenates, complicating separation.[42,50] These side reactions necessitate precise control of catalyst functionality and operating conditions to couple bond cleavage with hydrogenation while suppressing condensation.

Quantitative kinetic elucidation of these processes was pioneered by Zhang and co-workers,[32] who modeled glucose RAC over ammonium metatungstate (AMT) catalysts. Three consecutive reactions were identified: (R1) glucose RAC to erythrose and glycolaldehyde, (R2) erythrose RAC to glycolaldehyde, and (R3) self-condensation of glycolaldehyde to by-products.[62,63] The first step (R1) followed pseudo-first-order kinetics with an apparent activation energy of 141–149 kJ mol^{-1}, whereas R2 and R3 exhibited higher reaction orders (1.7 and 2.5) but lower activation energies (79.9 and 52.7 kJ mol^{-1}). These data indicate that condensation reactions are highly sensitive to glycolaldehyde concentration, emphasizing the need to maintain low steady-state intermediate levels.

Further refinement incorporated hydrogenation into the kinetic framework. Using an AMT-4% Ru/AC bifunctional catalyst, Zhang's group[33] identified hydrogenation of glucose to hexitols (R4) and of glycolaldehyde to EG (R5). Reaction R4 exhibited a first-order rate dependence[64] with an activation energy of 38 kJ mol^{-1}—about one-fourth that of RAC (R1). This disparity explains the observed trade-off between hexitol and EG selectivity with temperature.[65] As temperature increases, the endothermic RAC reaction accelerates faster than hydrogenation, improving EG yield but reducing sorbitol formation. Conversely, at lower temperatures, rapid hydrogenation locks glucose into inert polyols, halting further bond cleavage. Moreover, the condensation rate (R3, 2.5-order) increases more sharply with glycolaldehyde concentration than hydrogenation (R5, ~1.1-order), making intermediate levels control critical. In semi-continuous reactors, lowering the glucose feed rate from 10 to 2 mL min^{-1} increased EG yield from 17.7% to over 50%,[33] highlighting the importance of maintaining kinetic balance among sequential steps. The kinetic hierarchy—RAC slower than hydrogenation in low temperature but faster than condensation in low intermediate levels—thus defines the narrow temperature–concentration window for selective EG formation.

A Langmuir–Hinshelwood–Hougen–Watson (LHHW) model further clarified the surface reaction mechanisms of glucose and glycolaldehyde on Ru catalysts.[31] Under 373–403 K and 6 MPa H_2, the apparent activation energies for glycolaldehyde and glucose hydrogenation were 42.6 and 49.6 kJ mol^{-1}, respectively. However, the pre-exponential factor for glycolaldehyde was nearly four times larger, resulting in a significantly faster reaction rate. The addition of AMT modified the adsorption behavior. Strong AMT–Ru interactions ($K_{AMT} \approx 10^3$ to $10^4 \times K_G$) and formation of AMT-glucose complexes suppressed glucose hydrogenation by an order of magnitude, while the smaller glycolaldehyde was minimally affected. This competitive adsorption effect underpins the "self-selective hydrogenation" behavior observed in bifunctional catalysts, where acid–metal proximity dynamically regulates surface coverage and reaction order. Such kinetic self-regulation provides a molecular explanation for the dual-site synergy central to cellulose hydrogenolysis.

Building on intrinsic kinetics, Zhang *et al.*[66] developed a macroscopic model integrating six elementary steps—RAC, hydrogenation, thermal degradation, condensation, and EG gasification. The model quantitatively reproduced the yields of EG, hexitols, and gaseous products as functions of temperature, glucose concentration, and feed rate, and accurately predicted that low feed rates favor high EG yield, temperature elevation shifts selectivity from hexitols to EG, and excessive temperature and extremely low feed rate can trigger EG gasification. The strong agreement between simulation and experiment validated the kinetic scheme and provided a design basis for continuous hydrogenolysis reactors, enabling industrially relevant scale-up of cellulose-to-EG processes using high-solid slurries[67] or dual-stage systems coupling saccharification and hydrogenation.[68]

The hierarchy of activation energies explains why cellulose hydrogenolysis requires elevated temperatures. Hydrolysis of β-1,4-glycosidic bonds presents a high barrier (120–180 kJ mol^{-1}),[69,70] reinforced by a crystalline hydrogen-bonding network, while RAC of glucose to glycolaldehyde demands ~140 kJ mol^{-1},[71,72] and hydrogenation of sugars and intermediates proceeds more readily (~50 kJ mol^{-1}). Thus, reactions typically operate above 453 K.[24,25] Lowering the activation barriers of hydrolysis and RAC remains crucial for mild-temperature catalysis. Shuai *et al.*[73] developed a cellulase–mimetic sulfonated chloromethyl polystyrene resin (CP–SO_3H) catalyst, reducing the hydrolysis activation energy from 170 kJ mol^{-1} (H_2SO_4 catalysis) to 83 kJ mol^{-1} *via* cooperative –Cl/–SO_3H interactions. Sulfonated carbon catalysts containing phenolic hydroxyl and carboxyl groups achieved hydrolysis activation energies around 110 kJ mol^{-1},[74] highlighting the importance of hydrogen-bond disruption. However, analogous reductions in RAC activation energy have yet to be achieved, and current W-based Lewis acid systems remain dependent on temperatures above 453 K.

The convergence of kinetic modeling, spectroscopic evidence, and reactor validation has transformed cellulose hydrogenolysis from empirical observation into a quantitatively predictive science. These findings elucidate not only the relative energy barriers among hydrolysis, RAC, and hydrogenation but also how catalyst structure governs this energetics *via* site balance and adsorption dynamics. Looking forward, biomimetic strategies inspired by enzyme catalysis—constructing multifunctional active centers that mimic the cooperative binding and cleavage of cellulases and aldolases—represent a promising direction. Hybrid catalysts combining Sn–W acid pairs or metal–enzyme interfaces could reduce the activation barriers of both hydrolysis and C–C scission, enabling efficient diol production under mild conditions. These mechanistic

foundations underpin the selectivity-control strategies discussed in the following section.

2.3 Selectivity control in C–C and C–O bonds cleavage

Building upon the mechanistic and kinetic insights discussed above, product selectivity in cellulose hydrogenolysis fundamentally depends on the interplay between C–C and C–O bond transformations within the reaction network. The cascade proceeds through cellulose depolymerization, glucose and aldose/ketose intermediates, α-hydroxy aldehydes or ketones, and finally to alcohols such as ethanol, EG, and 1,2-PG. Each step competes dynamically with parallel processes, including isomerization, RAC, hydrogenation, dehydration, and over-hydrogenolysis, making product distribution highly sensitive to catalyst composition, active-site balance, and reaction microenvironment.

2.3.1 Regulation toward ethanol and EG. EG and ethanol share a common upstream chemistry, diverging primarily in the degree of reduction. Achieving high EG yield requires suppressing glucose isomerization to fructose to ensure direct RAC rather than tautomerization. Once this interference is removed, EG selectivity depends on the kinetic balance between deep hydrogenation to hexitols and RAC-hydrogenation coupling to EG. When hydrogenation dominates ($k_H \gg k_{RAC}$), glucose is over-reduced to unreactive hexitols; when cleavage dominates ($k_{RAC} \gg k_H$), condensation and degradation occur.[66] Optimal performance arises from a narrow kinetic "selectivity window" requiring precise metal–acid cooperation and microenvironment control.

Hydrolysis synchronization further governs this balance. Moderate hydrolysis that releases glucose at rates matching RAC and hydrogenation minimizes transient accumulation and polymerization. Zhao *et al.*[33] reported that lowering glucose feed rate from 10 to 0.67 mL min^{-1} increased EG yield from 17.7% to 53.4%, due to second-order glycolaldehyde condensation *versus* first-order hydrogenation kinetics. Operational variables such as temperature, hydrogen pressure, and residence time also critically influence selectivity. Raising temperature (453–518 K) enhances EG formation (from 14.6% to 60.0%) at the expense of hexitols (from 62.4% to 6.8%),[33] while both excessive and insufficient hydrogen pressure induce undesired condensation or over-hydrogenation.[75] Similarly, prolonged reaction time promotes re-hydrogenation and dehydration cycles, generating heavy polyols and humins.[76] Industrially, 4–6 MPa H_2 and 3–4 h residence achieve optimal trade-offs.

Solvent effects further tune selectivity by modulating hydrogen bonding and acid–metal balance. Methanol, for instance, weakens hydrogen-bonding networks and stabilizes α-hydroxy aldehydes,[77] shifting products toward EG and its monoethers, whereas water favors isosorbide formation.[57,78] Controlled oxidative atmospheres also provide selectivity tuning *via* redox-depth control, as Mo-based catalysts yield glycolic acid intermediates under O_2 that can be hydrogenated to EG.[79]

Beyond the aforementioned operational and solvent parameters, the selective control of the glucose RAC pathway is rooted in the microscopic realm of catalyst design and process kinetics. The initial C–C bond cleavage site in the glucose RAC reaction—either between C_2–C_3 or C_3–C_4—constitutes a critical branch point that determines the ultimate product distribution. This selectivity is governed primarily by the local active microenvironment of the catalyst. For instance, in tungsten-based catalysts,[32,33] the valence state and coordination structure of the W species modulate the surface acidity/redox properties, which in turn influence the adsorption mode of glucose and the activation of specific C–C bonds. When the catalytic sites favor preferential cleavage of the C_2–C_3 bond and stabilization of the glycolaldehyde intermediate, the reaction pathway is directed toward EG; conversely, cleavage at the C_3–C_4 bond promotes the formation of erythrose and subsequent C_4 products. Therefore, achieving directed pathway control fundamentally relies on atomic-level catalyst design to tailor the electronic and geometric structure of the active sites.

2.3.2 Regulation toward 1,2-PG. Selective formation of 1,2-PG requires efficient glucose-to-fructose isomerization before RAC, functioning as a mechanistic valve directing the pathway toward C_3 intermediates. Two complementary approaches are recognized: alkaline-assisted catalysis[80,81] and Sn-based Lewis acid catalysis.[82–85] In alkaline-assisted systems, hydroxide ions facilitate enediol rearrangement, while metal cations such as Ca^{2+} form cyclic transition states with glucose, stabilizing intermediates and lowering barriers for isomerization and RAC.[86–88] Sn-based Lewis acid sites, exemplified by framework Sn^{4+} in Sn-Beta zeolites, emulate enzymatic active centers through a "ring opening-isomerization-ring closing" cycle.[89,90] Compared with ZnO_x, CeO_x, or AlO_x systems, SnO_x exhibits stronger Lewis acidity, accelerating both isomerization and C–C scission.[82–85] These two mechanistic regimes—base-assisted and enzyme-mimetic—represent orthogonal yet potentially synergistic paradigms for maximizing C_3 selectivity. However, quantitative correlations between site distribution and kinetic selectivity remain underexplored.

2.3.3 Directional conversion among multiple alcohols. Beyond binary C_2/C_3 control, tuning catalyst composition enables targeted switching among ethanol, EG, 1,2-PG, and higher polyols. Product distributions are highly sensitive to the metal–acid ratio and interfacial electronic structure. As shown in Fig. 3,[43] Ni–W/SBA-15 catalysts exhibited EG yield peaks (~75%) at Ni/W = 1 : 3 and 1 : 5 but fell to 31.8% at Ni/W = 1 : 1, where hexitol formation dominates.[43,91] Similarly, Ni–Cu/WO_3 catalysts display compositional dependence. Increasing Cu shifts selectivity from EG to 1,2-PG and 1,2-butanediol (1,2-BDO).[92] In Pt-SnO_x/Al_2O_3 systems, increasing the Sn/Pt ratio suppresses over-hydrogenation, steering products toward C_2–C_3 alcohols.[83]

At the metal–support interface, tungsten dispersion critically affects selectivity. Highly dispersed WO_4 units and oligomeric WO_x clusters in Pd–WO_x/Al_2O_3 provide abundant Lewis acid sites, promoting glucose–fructose isomerization and enhancing 1,2-PG selectivity (~60.8%),[93] while poorly dispersed crystalline WO_3 phases reduce acid site density, weakening RAC-isomerization coupling and shifting selectivity toward EG (~45%).[94] Such dispersion-dependent tuning exemplifies how

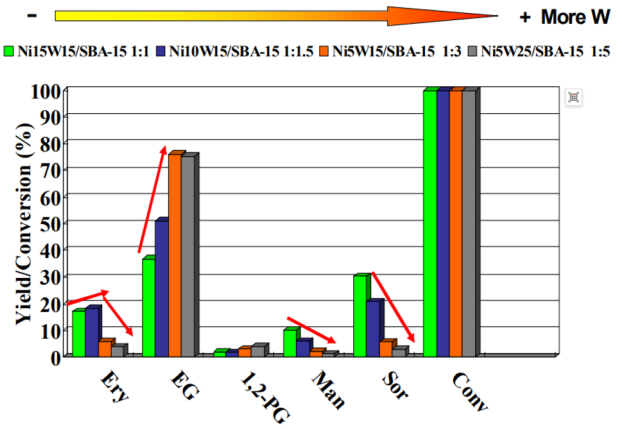

Fig. 3 The variation of product distribution on the Ni–W/SBA-15 bimetallic catalyst with the Ni/W mass ratio. Conv, Ery, EG, 1,2-PG, Mann, and Sor represent the cellulose conversion rate and the yields of erythritol, ethylene glycol, 1,2-propanediol, mannitol, and sorbitol, respectively. Reproduced with permission.[43] Copyright 2014, Elsevier.

atomic-level control over acid–metal proximity dictates C_2/C_3 product balance.

Collectively, these findings demonstrate that selectivity in cellulose hydrogenolysis arises from multiscale coupling—from electronic-level metal–acid interactions to reactor-scale concentration dynamics. Rational tuning of active-site composition, dispersion, and reaction microenvironment enables the precise steering of C–C and C–O bond cleavage, establishing a mechanistic platform for the sustainable synthesis of value-added, low-carbon alcohols. Nevertheless, maintaining long-term metal–acid synergy and structural integrity under continuous operation remains a key challenge for future development.

3 Catalyst design concepts

Building upon the mechanistic landscape outlined in Section 2, the following discussion focuses on how these principles are translated into concrete catalyst architectures. The central challenge in cellulose hydrogenolysis is not merely identifying active metals or acids, but engineering spatial and electronic cooperation among functional sites so that hydrolysis, C–C cleavage, and hydrogenation proceed in a controlled, mutually reinforcing sequence. Catalysts capable of achieving this synchronization combine hydrogenation-active metals with acid or redox functionalities that promote glycosidic bond activation and *retro*-aldol scission. The decisive factors are the density, proximity, and electronic alignment of these sites, which together determine whether reaction intermediates are channelled toward desired diols or diverted into condensation and over-hydrogenation.

The sections below examine how these mechanistic requirements are embodied across catalyst families—from noble metals that offer controlled hydrogen activation to base-metal systems that integrate bifunctional chemistry at lower cost. Tungsten-containing oxides, phosphates, and mixed-metal supports are discussed not as a separate class but as acidic and electronic modifiers that mediate metal–acid synergy. Finally, we consider structural strategies—confinement, interface engineering—that bridge intrinsic reactivity and reactor-scale performance.

3.1 Design principles derived from mechanistic insights

The mechanistic framework provides three practical descriptors that guide catalyst design for selective cellulose hydrogenolysis. First, site coordination and spatial intimacy govern reaction sequencing. Instead of simply co-locating metal and acid functions, modern catalysts aim to tune their distance and coupling strength so that reactive intermediates can migrate rapidly from cleavage to hydrogenation sites. Atomic-scale proximity, as achieved in Ru–W[71] or Ni–W[40] nanocomposites, minimizes the lifetime of unstable species such as glycolaldehyde, thus suppressing polymerisation without over-reducing glucose. Second, electronic modulation translates mechanistic selectivity into tunable reactivity. Interfacial charge redistribution between metal and oxide components controls hydrogen adsorption and carbonyl activation. This concept underpins systems such as Pt–SnO_x[83] and Ni–W,[40] where tailored electronic interaction balances hydrogenation power with cleavage activity, ensuring kinetic alignment across the cascade. Third, mesoscale architecture provides the physical environment for sustaining these interactions. Hierarchical porosity, oxide confinement, and hydrophilic–hydrophobic interfaces regulate molecular transport and stabilize transition states. By manipulating local polarity and solvent accessibility, the same active composition can exhibit markedly different selectivity toward EG or 1,2-PG.

Together, these design parameters—site coordination, electronic modulation, and mesoscale environment—offer a transferable framework that links molecular understanding to catalyst engineering. They set the stage for analyzing how different metal systems realize these principles in practice.

3.2 Noble metal catalysts

Noble metals, particularly Ru, Pd, and Pt, represent the benchmark hydrogenation components for aqueous-phase cellulose hydrogenolysis, combining high intrinsic H_2 activation ability with tunable chemoselectivity toward C–O and C–C bond cleavage. Their function is primarily associated with the activation of molecular hydrogen and the selective hydrogenation of reactive intermediates such as glycolaldehyde and glyceraldehyde, which would otherwise undergo condensation in aqueous media. When coupled with acid or oxophilic promoters, these metals enable efficient cascade conversion of cellulose to low-carbon alcohols under comparatively mild conditions.

3.2.1 Ru-based catalysis. Ruthenium remains the prototypical noble metal for catalytic hydrogenolysis of cellulose and its derivatives, combining moderate hydrogenation strength, high dispersion on acid or redox supports, and exceptional hydrothermal stability. These features make Ru-based systems the benchmark for elucidating bifunctional mechanisms that couple metallic hydrogenation with acid- or oxide-promoted C–O and C–C bond cleavage. Over the past two decades,

systematic investigations from solid cellulose to monosaccharides and polyols have established a coherent mechanistic picture linking active-site architecture, interfacial redox chemistry, and product selectivity.

Cellulose hydrogenolysis. Early demonstrations of direct cellulose hydrogenolysis highlighted the feasibility of one-pot hydrolytic hydrogenation under hydrothermal conditions. Fukuoka and Dhepe first achieved 31% hexitol yield (25% sorbitol, 6% mannitol) with Pt/γ-Al_2O_3 at 190 °C.[25] Building on this concept, Luo *et al.*[24] showed that Ru/C at 245 °C enabled hydrolysis through proton generation from subcritical water, yielding ∼30% sorbitol. These studies established the conceptual basis for green cellulose valorization but also revealed the necessity of bifunctional catalysts capable of balancing hydrolysis, RAC, and hydrogenation steps.

Integration of Ru with tungstate or acidic components has proven crucial for orchestrating these elementary reactions, as shown in Table 1. Fu *et al.*[95] prepared Ru–WO_x/HZSM-5, producing 42.3% ethanol at 235 °C after 24 h, attributed to highly dispersed Ru_3W_{17} alloy species and the moderate acid sites with HZSM-5, which together balanced C–O and C–C scission. Comparative evaluations by Li *et al.*[96] among (Pd, Pt, Rh, Ru, Ir)/WO_3 on rectangular WO_3 nanosheets identified 1% Ru/WO_3 as the most active, yielding 76.3% EG at 240 °C, 4 MPa H_2 within 2 h. The high activity was ascribed to interfacial W^{5+}/$RuO_x^{\delta+}$ sites that simultaneously promoted RAC and hydrogenation. Similarly, Wiesfeld *et al.*[97] found 2% Ru/tungstate delivering 61% EG at 225 °C, 4.5 MPa H_2, and 1 h, confirming the universality of Ru–W cooperative effects.

Zheng *et al.*[71] systematically compared Pd–W/AC, Pt–W/AC, Ru–W/AC, and Ir–W/AC under identical conditions, revealing that Ru–W/AC afforded the highest EG selectivity (61.7%) and emphasizing the critical role of Ru–W synergy. Fabičovicová *et al.*[98] demonstrated that Ru/W/AC converted microcrystalline cellulose with 84% polyol yield and raw biomass (pine, birch, eucalyptus), confirming scalability. Ribeiro *et al.*[99] achieved 40% EG at 205 °C, 5 MPa H_2 with 0.8% Ru–30% W/CNT, outperforming monometallic counterparts and their physical mixtures. HNO_3-oxygenated CNT surfaces enhanced hydrolysis and suppressed glucose isomerization.[100] Replacing common CNTs with hydrothermal glucose-derived carbon supports (CG and CG-CNT) delivered 48% EG yield at lower cost.[101] Graphene-based composites further improved performance *via* extended π networks and functional group cooperation.[102] Carboxyl (–COOH) sites promoted hydrolysis, while hydroxyl (–OH) groups stabilized glycosidic oxygens. Zhang *et al.*[103] reported 5% Ru–30% $W_{18}O_{49}$/graphene achieving 62.5% EG at 245 °C and 6 MPa H_2 within 1 h, attributed to Ru cluster-$W_{18}O_{49}$ nanowire synergy and interfacial charge transfer.

Acidic and heteroatom-functionalized supports have also proven effective for stabilizing Ru nanoparticles and modulating acidity. Ru/AC–SO_3H retained ∼71% sorbitol yield after five cycles,[104] while Ru_2P/C–SO_3H achieved 64% sorbitol *via* moderated H adsorption.[105] Ru loading optimization (3 wt%) on sulfonated carbon maximized hexitol yield (44.5%) at 94.8% cellulose conversion.[106,107] Diverse acidic supports, including Ru/Al_2O_3,[108] Ru/$NbOPO_4$,[109] Ru/BEA zeolite,[110] Ru/MCM-48,[111] Ru/MN-270 (highly cross-linked polystyrene),[112] Ru/$Cs_3HSiW_{12}O_{40}$,[113] exhibited 50–70% sorbitol selectivity with excellent hydrothermal stability. In temperature-responsive phase-transfer systems, Ru/AC combined with H_2WO_4 achieved 54.4% EG yield with negligible loss over 20 cycles, as H_2WO_4 dissolved and reprecipitated reversibly.[114] Likewise, Ru/C coupled with WO_3/ZrO_2 exhibited enhanced activity (52.9% EG at 215 °C, 5.2 MPa H_2) due to surface W^{5+}–OH species acting as active C–C scission centers.[115]

The introduction of additional acid components can further lower the activation barrier for cellulose hydrolysis by protonating glycosidic oxygens.[116] Heteropoly acids (HPAs) have been particularly effective as co-catalysts, providing strong Brønsted acidity and facile regeneration.[117,118] For instance, Ru/SBA-15 coupled with $H_3PW_{12}O_{40}$ achieved 55.5% EG selectivity,[119] while Ru/C + HPA/ZrO_2 yielded 40% EG and 26.2% hexitols after ball-milling pretreatment of cellulose.[120] Palkovits *et al.*[121] reported that $H_4[Si(W_3O_{10})_4]$ and Ru/C achieved >81% cellulose conversion and 65% sugar–alcohol yield from spruce wood, demonstrating excellent activity and recyclability. Acid-assisted systems such as Ru/C + 0.10 M HCl,[122] Ru/CNT + H_3PO_4,[123] and Ru/H-USY + HCl[124] also afforded 49.5% isosorbide, 69% sorbitol, and ∼90% hexitols yield, respectively. HPAs offer the added benefits of high selectivity, low corrosion, and easy recovery,[125] affording >50% isosorbide from cellulose and 63% from wheat-straw pulp.[126]

Nano-structural and compositional engineering have provided further means of optimizing activity and selectivity. Yang *et al.*[127] developed a yolk–shell Ru/NC@void@MC-SO_3H catalyst featuring 1.4 nm Ru clusters confined within sulfonated mesoporous carbon. This catalyst yielded 38% 1,2-PG and productivity of 342.86 mol h^{-1} g_{Ru}^{-1}, with –SO_3H groups facilitating hydrolysis, Ru–N_x pairs promoting isomerization and RAC, and Ru^0 sites hydrogenating intermediates—an elegant example of spatially cooperative catalysis. Crystal-phase engineering of WO_3 also governs activity.[128–131] Hexagonal (h-WO_3) exposing (100) planes and retaining structural H_2O forms H_x-$WO_3 \cdot H_2O$[132] acid centers that enhance both hydrolysis and RAC, giving 77.5% EG at 240 °C, 4 MPa H_2 and 2.0 h.[133]

Mechanical and interfacial engineering have also advanced sorbitol productivity. Ball-milling Ru/CNT or Ru/AC with cellulose enhanced contact and crystallinity reduction, increasing sorbitol selectivity to ∼80%.[134,135] Incorporation of Ni produced Ru–Ni bimetallic catalysts that exhibited electronic synergy and additional hydrogenation functionality, affording 50–70% sorbitol depending on Ni content.[136] N-doped carbon supports further enhanced Ru dispersion and modulated adsorption properties.[137,138] Ru–N/AC-1.3 produced 82% sorbitol, with DFT indicating that pyridinic–*N* modulates Ru adsorption energy, balancing glucose activation and product desorption.[139]

To facilitate catalyst recovery and long-term stability, magnetic Ru systems have been developed. Lai *et al.*[140] reported a magnetic sulfonated mesoporous SiO_2 catalyst for the hydrolysis of biomass to glucose. Fe_3O_4@C–SO_3H core–shell systems combined acidity and magnetic recoverability.[141] Ru–Fe_3O_4–SiO_2 achieved 19% EG and 20% 1,2-PG selectivities at 255 °C, where Fe_3O_4 modulated the Ru^0/Ru^{4+} ratio.[142,143] Lv *et al.*[144]

Table 1 Ru-based catalytic systems for conversion of cellulose to low-carbon alcohols in aqueous systems

Entry	Catalyst	T (°C)	P (MPa, H_2)	T (h)	Yield (C mol%)	Ref.
1	Ru/C	245	6.0	0.1	Sorbitol 30	24
2	Ru–W/AC	245	6.0	0.5	EG 61.7	71
3	50% WO_3/Al_2O_3 + Ru/C	245	6.0	0.5	EG 16.6 1,2-PG 30.7	94
4	5Ru–25WO_x/HZSM-5	235	3.0	24.0	Ethanol 42.3	95
5	1% Ru/WO_3	240	4.0	2.0	EG 76.3	96
6	2% Ru/tungstate	225	4.5	1.0	EG 61.0	97
7	Ru/W/AC	220	6.5	3.0	EG 34.2 Sorbitol 18.5	98
8	0.8% Ru–30% W/CNT	205	5.0	3.0	EG 40.0	99
9	Ru/CNT_{HNO_3} + W/CNT	205	5.0	5.0	EG 41.0	100
10	Ru/CG_{HNO_3} + W/CG	205	5.0	5.0	EG 48.4	101
11	5% Ru–30% $W_{18}O_{49}$/graphene	245	6.0	1.0	EG 62.5	103
12	Ru/AC–SO_3H	165	5.0	24.0	Sorbitol 71	104
13	2 wt% Ru_2P/C–SO_3H	200	3.0	2.0	Sorbitol 64	105
14	3 wt% Ru/AC–SO_3H	180	2.0	24.0	Hexitols 44.5	106
15	Ru/Al_2O_3	190	5.0	24.0	Sorbitol 53.2	108
16	$Ru/NbOPO_4$	170	4.0	24.0	Sorbitol 50–60	109
17	3 wt% Ru/BEA zeolite	180	1.6	3.0	Sorbitol 72.8	110
18	Ru/MCM-48	200	5.0	0.1	Hexitols 48.5	111
19	1% Ru/MN-270	245	6.0	0.1	Hexitols 50	112
20	1% $Ru/Cs_3HSiW_{12}O_{40}$	180	5.0	3.0	Sorbitol 59	113
21	Ru/AC + H_2WO_4	245	6.0	0.5	EG 54.4	114
22	Ru/AC + WO_3/ZrO_2	215	5.2	1.5	EG 52.9	115
23	Ru/SBA-15 + $H_3PW_{12}O_{40}$	245	5.0	4.0	EG 55.5	119
24	Ru/C + $H_3PW_{12}O_{40}/ZrO_2$	220	5.0	5.0	EG 40.0 Hexitols 26.2	120
25	Ru/C + $H_4[Si(W_3O_{10})_4]$	160	5.0	7.0	C yield 90	121
26	Ru/C + 0.10 M HCl	215	6.0	0.5	Isosorbide 49	122
27	Ru/CNT + H_3PO_4	185	5.0	24.0	Sorbitol 69	123
28	Ru/H-USY + HCl	190	5.0	24.0	Hexitols 90	124
29	Ru/C + $H_4SiW_{12}O_{40}$	180	5.0	24.0	Hexitols 86	125
30	Ru/C–$H_4SiW_{12}O_{40}$	210	5.0	1.0	Isosorbide 50–63	126
31	Ru/NC@void@MC–SO_3H	230	6.0	5.0	1,2-PG 38.0	127
32	1% Ru/h-WO_3	240	4.0	2.0	EG 77.5	133
33	Ru/CNT	205	5.0	5.0	Sorbitol 60	134
34	Ru/AC	205	5.0	5.0	Sorbitol 80	135
35	Ru–Ni/AC or Ru–Ni/CNT	205	5.0	5.0	Sorbitol 50–70	136
36	Ru–N/AC-1.3	200	3.0	2.0	Sorbitol 82	139
37	Ru–Fe_3O_4–SiO_2	255	6.0	0.8	EG 19.0 1,2-PG 20.0	143
38	Fe_3O_4@SiO_2/10% Ru–20% WO_x	245	5.0	2.0	1,2-PG 32.4	144
39	3 wt% Ru/C + 6 wt% WO_3/C	205	6.0	0.5	EG 14.6 1,2-PG 3.7	145
40	Ru/CNT	170; 205	5.0	2.0; 4.0	Sorbitol 75 Xylitol 77	146
41	Ru/AG-CNT	205	5.0	3.0	Sorbitol 64.1	147
42	Ru/CNT	205	5.0	5.0	Sorbitol 50	148

optimized Ru–WO_x ratios on magnetic Fe_3O_4@SiO_2 supports, obtaining 32.4% 1,2-PG yield. In dual-bed configurations, spatial separation of cleavage and hydrogenation zones (50% WO_3/Al_2O_3 and Ru/C) afforded 16.6% EG and 30.7% 1,2-PG at 245 °C, 6 MPa H_2 and 0.5 h,[94] while significant variations in the distribution of diol products over Ru/C and WO_3/C.[145]

Monosaccharides and polyols hydrogenolysis. As the monomeric unit of cellulose, glucose and its isomer fructose represent central intermediates linking polysaccharide and polyol hydrogenolysis. Their aqueous-phase transformation bypasses solid-state hydrolysis, offering higher conversion efficiency under mild conditions.[149,150] Among various systems, Ru–W systems again dominate owing to robust metal–acid cooperation that regulates RAC *versus* hydrogenation. Zhang *et al.*[151] found that tungstate species dramatically enhanced C–C cleavage, following the order H_2WO_4 > HPW > WO_3 > AMT > HSiW. PEG-modified Ru–W catalysts yielded 35.2% EG, 27.1% 1,2-PG, and 31.1% 1,2-BDO in continuous operation,[152] while tuning W oxidation states (W^{4+} *vs.* W^{5+}) shifted selectivity from mixed diols (87%) to EG (56%)[153] and 1,2-BDO (72.1%).[154]

Magnetic Fe_3O_4@SiO_2/10% Ru-20% WO_x produced 30.8% 1,2-PG;[144] 5% Ru/C + ZnO gave 38% PG at 180 °C and 0.4 MPa H_2;[155] and RuSn/AC with balanced alloy–oxide interfaces afforded 25% 1,2-PG and 26.9% EG.[156] These findings demonstrate that Ru–W interfacial redox state and secondary oxide modifiers determine branching between C_2 and C_3 products. In addition, extensive screening of Ru catalysts[157–160] and their loading on carbon,[161,162] SiO_2,[163] Al_2O_3,[164] NiO–TiO_2,[165,166] zeolites,[167–169] and ordered mesoporous silicas[149] shows that activity and stability are governed by metal–support intimacy and surface acidity. Bimetallic RuNi/MCM-48 (Ru/Ni = 0.45)[168] and 1% Ru/HY[169] afford >98% sorbitol selectivity with good reusability, while sol–gel $(RuO_2)_{0.038}\cdot(SiO_2)_{0.962}$[149] and polymer-encapsulated Ru/ASMA@AC[170] exhibit increasing activity and stability, and the latter can steady 99.7% glucose conversion and 93% sorbitol selectivity over multiple cycles. The decisive stability factor is the strength and homogeneity of Ru–support interactions engineered during synthesis.

Fructose, more reactive than glucose, provides a direct entry to C_3 polyols *via* RAC reaction to glyceraldehyde/dihydroxyacetone and subsequent hydrogenation.[171,172] Under AMT-4% Ru/AC, 37.9% 1,2-PG was obtained at 240 °C, 5 MPa H_2;[33] Fe_3O_4@SiO_2/10% Ru–20% WO_x yielded 33.4% 1,2-PG;[144] 3 wt% Ru/C + WO_3 gave 47.9% 1,2-PG at 205 °C, 6 MPa H_2;[94] and Ru–WO_x/hydroxyapatite (HAP) produced 91.3% 1,2-PG at 180 °C, 1 MPa H_2,[172] attributed to highly dispersed Ru and WO_x on weakly basic sites that facilitate RAC and suppress humin formation. These consistent results emphasize that fine control of acidity and metal dispersion governs whether glucose or fructose routes dominate diol selectivity.

Beyond monosaccharides, Ru-based catalysts are also highly effective for the hydrogenolysis of sugar alcohols such as sorbitol and xylitol—representative intermediates bridging carbohydrate conversion and polyol production. These reactions typically proceed through sequential dehydrogenation, RAC, and hydrogenation steps (Fig. 4).[173] On Ru surfaces, sorbitol dehydrogenation initiates at the C(5)–H bond,[173] followed by retro-aldol cleavage at either the C_3–C_4 or C_2–C_3 position to yield 1,2-PG or EG, respectively. The product ratio depends sensitively on catalyst basicity and the electronic state of Ru.[174] Mechanistic studies have confirmed that C–C bond scission predominantly follows the RAC pathway under both neutral and alkaline conditions, with moderate basicity accelerating the rate and shifting selectivity toward diols.[175,176] Zhou *et al.*[177] achieved 58.6% diol selectivity at 220 °C, 8 MPa H_2 with 3% Ru/CNF (carbon nanofiber), while Ru–CNF/graphite-felt hybrids gave 79.1% toward EG, 1,2-PG, and glycerol.[178] Continuous trickle-bed tests[179] showed that optimizing mass transfer and catalyst-layer thickness maximized diol selectivity.

In alkaline media, Ru catalysts supported on basic oxides or co-promoted by $Ca(OH)_2$ exhibit enhanced stabilization of enolate intermediates and improved C–C bond cleavage activity. For instance, $Ru_{0.25}WO_x$/CNTs with $Ca(OH)_2$ delivered 60.2% combined EG with 1,2-PG at 205 °C,[180] and surface functional groups of CNT enhanced Ru dispersion and adjusted acidity/basicity.[181] Similarly, bifunctional acid–metal systems such as Ru/Al_2O_3 have delivered superior diol selectivity due to moderate acidity, appropriate Ru/Al ratios, and partially oxidized Ru species.[182] Mechanistically, Ru initiates dehydrogenation and C–C cleavage, while basic or acidic co-catalysts stabilize reactive intermediates and regulate electron density—together dictating the EG *versus* 1,2-PG selectivity landscape.

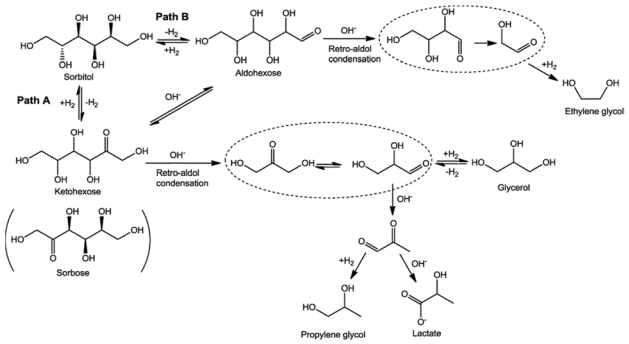

Fig. 4 The proposed reaction pathway for the hydrogenolysis of sorbitol to produce C2 and C3 products in the presence of alkaline and metal catalysts. Reproduced with permission.[173] Copyright 2016, the Royal Society of Chemistry.

Across cellulose, monosaccharide, and polyol transformations, Ru-based catalysts display a unifying mechanistic motif. Cooperative interaction between metal and acid/base sites governs the sequence of bond-cleavage and hydrogenation steps leading to low-carbon polyols. W-containing supports and Brønsted or Lewis acids synchronize RAC and hydrogenation, alloying and redox tuning modulate electron density at Ru sites, and structural confinement ensures stability under hydrothermal conditions. Despite significant advances, challenges remain in correlating Ru oxidation dynamics with turnover frequencies and in designing scalable catalysts that maintain metal–acid/base balance during long-term operation. Future progress will hinge on integrating operando spectroscopy and kinetic modeling to link interfacial structure with product selectivity, translating the mechanistic foundation of Ru-based systems into predictive catalyst design principles for sustainable polyol production.

3.2.2 Pd-based catalysis. Palladium catalysts possess relatively weaker hydrogenolytic strength than ruthenium but exhibit superior chemoselectivity, sintering resistance, and hydrothermal durability. Their tunable electronic structure and strong compatibility with oxide and tungstate supports make Pd-based systems attractive candidates for selective C–C and C–O bond activation in biomass valorization. Current research converges on three main domains—direct cellulose hydrogenolysis to ethanol and EG, glucose/fructose conversion to diols, and sugar-alcohol hydrogenolysis—each highlighting how Pd's adjustable metal–acid interface enables selective cascade transformations under aqueous conditions, as shown in Table 2.

Cellulose hydrogenolysis. Early studies confirmed the viability of Pd as the hydrogenation component in bifunctional cellulose hydrogenolysis. Chu *et al.*[27] developed a multifunctional Pd–Cu–WO_x/SiO_2 catalyst that converted corn stover-derived

cellulose to ethanol in a one-pot process, yielding 42.5C % ethanol at 300 °C and 4 MPa H_2. The synergy among Pd, Cu, and WO_x enabled sequential hydrolysis, RAC, and hydrogenation under relatively mild hydrothermal conditions. Gumina *et al.*[183] further demonstrated Pd/Fe_3O_4 catalysis without external hydrogen, attaining 51% ethanol selectivity after 12 h through *in situ* H_2 generation *via* water dissociation. A Pd–W_2C/C composite yielded 58.2% EG at 220 °C and 4 MPa H_2, demonstrating the cooperative hydrogenation-RAC function of Pd and W_2C.[184]

Particle-size and morphological effects further modulate electronic structure and metal–acid synergy. Jia *et al.*[185] synthesized Pd/WO_x catalysts with particle sizes from 1.81 to 4.46 nm and discovered a volcano-type relationship, with ~3.0 nm Pd particles affording the highest total C_2 alcohol yield (78.5%, including 61.2% EG and 17.3% ethanol at 230 °C and 5 MPa H_2). Smaller clusters exhibited abundant oxygen vacancies but insufficient hydrogenation activity, while larger Pd domains lost metal–acid synergy. Morphological control of WO_3 further optimized this balance. Pd supported on orthorhombic WO_3 (Pd/*o*-WO_3) produced 64.8% EG and 16.1% ethanol at 245 °C and 5.5 MPa H_2, due to the abundance of crystalline defects attributable to the formation of W^{5+}–OH species as well as the Pd–O(H)–W linkages that enhanced both acidity and hydrogenation.[186]

Bimetallic and nanostructured Pd systems further extend catalytic versatility. Pd–Fe/CNTs catalysts exhibited 55% total polyols and ~20% 1,2-PG at 240 °C and 6 MPa H_2, where charge transfer from Fe to Pd downshifted the Pd d-band center, suppressing over-hydrogenation and improving C–C cleavage selectivity.[187] Core-shell Pd@W/Al-$MSiO_2$ nanostructures achieved 96.1% cellulose conversion and 56.5% EG selectivity, with the W component leading to the formation of extra-framework Al species and increasing acidity, while the mesoporous shell prevented Pd sintering, retaining 48.5% EG selectivity after five cycles.[188] Similarly, encapsulated Pd@Al–SiO_2 catalyst featuring Lewis-acidic silicate shells afforded 59.3% ethanol selectivity,[189] whereas confined PdZn@Silicalite-1 structures reached 69.2% ethanol selectivity.[190] Collectively, these results establish that despite its weaker intrinsic hydrogenolysis activity relative to Ru, Pd can achieve comparable diol yields when integrated with well-defined supports and finely tuned acid–metal interfaces.

Monosaccharides and polyols hydrogenolysis. Monosaccharides such as glucose and fructose serve as crucial intermediates bridging cellulose depolymerization and polyol hydrogenolysis. Their aqueous-phase conversion provides mechanistic insight into C–C scission and hydrogenation. Xin *et al.*[191] prepared core–shell Pd@WO_x–$MSiO_2$ nanostructures and demonstrated that Pd@1.5% WO_x–$MSiO_2$ exhibited 59.4% EG selectivity at 200 °C and 5 MPa H_2. In this system, W^{5+}-derived oxygen vacancies facilitated glucose retro-aldol cleavage, followed by hydrogenation on Pd sites. Lv *et al.*[192] tuned the acidity of Pd@Al–$MSiO_2$ by varying Al content. Tetracoordinated AlO_4 sites introduced strong Lewis acidity, promoting glucose isomerization to fructose. Pd@Al_3–$MSiO_2$ achieved 95.4% glucose conversion and 45.2% 1,2-PG yield at 200 °C and 5 MPa H_2. Such spatially integrated Lewis-acid and Pd-metal sites effectively couple isomerization, RAC, and hydrogenation.

Support composition also dictates the acid–metal balance and, consequently, product distribution. Liu *et al.*[93] studied Pd-WO_x/Al_2O_3 catalysts with varying WO_x loadings and found that isolated WO_4 and oligomeric WO_x species, together with AlO_4 sites, provided abundant Lewis acidity, favoring glucose–

Table 2 Pd-based catalytic systems for conversion of cellulosic biomass to low-carbon alcohols in aqueous systems[a]

Entry	Catalyst	*T* (°C)	*P* (MPa, H_2)	*T* (h)	Yield (C mol%)	Ref.
1	Pd–Cu–WO_x/SiO_2	300	4.0	10.0	Ethanol 42.5	27
2	Pd/Fe_3O_4	240	0.5 N_2	12.0	Ethanol 51.0	183
3	2Pd–W_2C/C	220	4.0	2.5	EG 58.2	184
4	3Pd/WO_x	230	5.0	4.0	EG 61.2 Ethanol 17.3	185
5	Pd/*o*-WO_3	245	5.5	4.0	EG 64.8 Ethanol 16.1	186
6	Pd–Fe/CNTs (Pd : Fe = 1 : 1)	240	6.0	2.0	1,2-PG 20.0 Hexitols ~18.0	187
7	Pd@W/Al–$MSiO_2$	240	4.0	2.0	EG 56.5	188
8	Pd@Al–SiO_2	245	4.5	4.0	Ethanol 59.3	189
9	PdZn@silicalite-1	245	4.5	4.0	Ethanol 69.2	190
10	Pd–WO_x/Al_2O_3	180	4.0	WHSV 0.48 h^{-1}	1,2-PG 56.1 and 62.2	93
11	Pd@WO_x–$MSiO_2$	200	5.0	2.0	EG 59.4	191
12	Pd@Al–$MSiO_2$	200	5.0	3.0	1,2-PG 45.2	192
13	Pd/C–Zn/ZnO	250	/	0.5	1,2-PG 33.3	197
14	Pd/ZrO_2 + ZnO + Mg_3AlO_x	220	5.0	1.5	EG 1,2-PG 54.6	198
15	Pd–Cu/ZrO_2 + $La(OH)_3$	220	5.0	4.0	EG 15.9 1,2-PG 37.0	199

[a] Entries 1–9 used cellulose as the feedstock, entries 10–13 used glucose or fructose as the feedstock, and entries 14 and 15 used sorbitol as the feedstock.

fructose isomerization and subsequent RAC to C_3 intermediates. These intermediates were then hydrogenated on Pd sites to form 1,2-PG, achieving 92.2% conversion and 56.1% yield. The synergistic role of Al_2O_3 was further supported by the studies,[193,194] which established that WO_x/Al_2O_3 interactions lead to two-dimensional oxide overlayers whose acidity can be finely tuned by surface W density.[195,196] Comparative experiments confirmed that fructose conversion over Pd–WO_x (5%)/Al_2O_3 was more selective toward 1,2-PG (62.2% at 180 °C and 4 MPa H_2) than glucose under identical conditions,[93] consistent with fructose's intrinsically lower isomerization barrier. Using Pd@Al_3–$MSiO_2$, fructose conversion achieved 47.4% 1,2-PG yield.[192]

Alternative hydrogen sources have also been explored. Wang *et al.*[197] employed Pd/C–Zn/ZnO systems, where Zn promoted water dissociation to supply reactive hydrogen and simultaneously generated ZnO that enhanced glucose isomerization and fructose RAC, yielding 33.3% 1,2-PG at 250 °C within 0.5 h. These findings highlight that Pd-based Lewis-acid systems can finely direct the isomerization–cleavage–hydrogenation cascade toward C_3 products under moderate conditions.

Beyond monosaccharides, Pd catalysts are also active in sugar–alcohol hydrogenolysis. Jia *et al.*[198] employed a Pd/ZrO_2 + ZnO hybrid system, forming *in situ* PdZn alloys through physical mixing for the hydrogenolysis of sorbitol using Mg_3AlO_x as a solid base. At 220 °C and 5 MPa H_2, EG and 1,2-PG yields reached 54.6%. Activity and selectivity were strongly dependent on the amounts of ZnO and the solid base, which controlled the extent of alloy formation and modulated competition between base-catalyzed and metal-catalyzed steps. In a related study,[199] a bimetallic Pd–Cu/ZrO_2 catalyst in the presence of $La(OH)_3$ achieved 15.9% EG and 37.0% 1,2-PG at 220 °C and 5 MPa H_2. Electronic interaction between Pd and Cu inhibited excessive hydrogenation and maintained high stability during recycling. These findings collectively demonstrate that the introduction of secondary metals and solid bases enables Pd catalysts to efficiently mediate polyol hydrogenolysis by balancing metallic and basic functionalities.

Overall, Pd-based catalysts unite structural stability with adjustable hydrogenation strength and finely tunable acidity, providing a versatile platform for selective C–C and C–O bond activation. Their catalytic behavior depends critically on particle size and morphology (governing Pd^0/Pd^{2+} balance), interfacial acid–metal structure (particularly at Pd–WO_x or Pd–AlO_4 junctions), and synergistic promotion by secondary metals or bases (Cu, Zn, Mg_3AlO_x, $La(OH)_3$). Properly engineered Pd systems rival Ru catalysts in selectivity toward ethanol, EG, and 1,2-PG, yet offer superior recyclability and hydrothermal robustness, positioning them as promising candidates for continuous, scalable polyol production in aqueous-phase biomass conversion.

3.2.3 Pt-based catalysis. Platinum-based catalysts exhibit strong hydrogenolytic activity, exceptional resistance to sintering, and outstanding hydrothermal stability, making them efficient systems for selective C–C and C–O bond cleavage in biomass-derived polyols. Although less extensively explored than Ru-based systems, Pt catalysts show distinctive behavior arising from their strong metal–support interactions (SMSI), tunable oxidation states, and versatile electronic structures at metal–oxide interfaces. These attributes allow Pt-based catalysts to operate as adaptive bifunctional systems, coupling metallic hydrogenation with acid-, base-, or redox-promoted C–C/C–O scission under aqueous-phase conditions.

Cellulose hydrogenolysis. Early studies demonstrated that Pt supported on reducible oxides can drive direct cellulose hydrogenolysis through cooperative acid–metal catalysis. Zhang and co-workers first reported Mo/Pt/WO_x catalysts for one-pot cellulose conversion to ethanol under hydrothermal conditions, achieving 43.2% ethanol selectivity.[26] The O_xMo–Pt–WO_x interface created highly active sites for C–O bond cleavage in EG intermediates, facilitating subsequent hydrogenation. Similarly, Song *et al.*[28] found that H_2WO_4–Pt/ZrO_2 produced 32% ethanol under aqueous medium, where H_2WO_4 promoted glucose fragmentation *via* selective C–C cleavage and Pt/ZrO_2—featuring a balanced Pt^0/Pt^{2+} ratio—enabled controlled hydrogenolysis. Wu *et al.*[30] further demonstrated that combining Pt/WO_x with hollow Pt@HZSM-5 generated 54.4% yield of ethanol, underscoring the importance of spatial integration between Lewis acid and metallic sites in cascade cellulose hydrogenolysis.

Strong metal–support interactions play a defining role in regulating Pt catalytic behavior. Deng *et al.*[83] examined Pt-SnO_x/Al_2O_3 catalysts with different Sn/Pt ratios and observed a volcano-shaped dependence of selectivity on composition. At low Sn/Pt ratios (0.1–1.0), electron transfer from SnO_x to Pt enhanced hydrogenation, favoring hexitol formation (82.7% at Sn/Pt = 0.5). Higher ratios (>1.5) promoted C_2–C_3 diols such as EG and 1,2-PG, as detached $Sn(OH)_2$ species provided Lewis acidity for glucose isomerization and RAC reaction. Yang *et al.*[200] achieved 34.3% EG and 37.1% 1,2-PG (73.9% total alcohol yield) using Pt/CNT catalysts at 240 °C and 2 MPa H_2, while Wang *et al.*[201] synthesized Pt/RGO *via* microwave-assisted reduction to produce 58.9% sorbitol yield, attributed to optimized 3.6 nm Pt particles and efficient hydrogen spillover across the reduced graphene network. These examples illustrate how tuning oxidation state, support conductivity, and interfacial chemistry governs product selectivity and catalyst longevity.

Beyond oxide and carbon supports, hybrid systems combining homogeneous and heterogeneous functions have been developed to improve activity and stability. Girard *et al.*[202] employed $CeCl_3 \cdot 7H_2O$ as a co-catalyst with Pt/$BaZrO_3$, achieving 40.9% total yield of EG and PG, though Ba leaching and coking limited recyclability. Gu *et al.*[203] introduced a self-alkaline Pt/SiO_2@$Mg(OH)_2$ system, where $Mg(OH)_2$ acted as an intrinsic base to drive glucose isomerization and RAC. The catalyst produced 53.8% 1,2-PG at 180 °C and 6 MPa H_2 within 4 h, benefiting from synergistic effects between basic and metallic functions. These findings demonstrate the potential of integrating acid–base components within Pt frameworks to regulate the reaction microenvironment and sustain selectivity.

Monosaccharides and polyols hydrogenolysis. Pt-based catalysts are also highly active in the hydrogenolysis and hydrodeoxygenation of monosaccharides and sugar alcohols, particularly sorbitol. Huber and co-workers[55] identified key

intermediates in sorbitol hydrodeoxygenation over Pt/SiO_2–Al_2O_3, showing that C–C bond cleavage (*via* RAC and decarbonylation) occurred predominantly on acid sites, while C–O scission was catalyzed on Pt sites. The reaction followed dual pathways: intramolecular dehydration-cyclization forming cyclic C_6 species and RAC yielding C_3 polyols such as glycerol and 1,2-PG. Duprez *et al.*[204] systematically investigated the effect of the aqueous medium on Pt/SiO_2–Al_2O_3 catalysts under hydrothermal conditions (225 °C, 2.5 MPa, H_2O), revealing that prolonged exposure altered both metal dispersion and support acidity. Subsequent work[205] demonstrated that tuning the metal/acid ratio directly influenced selectivity. Higher Pt loadings favored C–C cleavage and hydrogenation, while excessive acidity led to over-dehydration.

To improve stability and tunability, bifunctional Pt/ZrO_2 and TiO_2–WO_x systems were developed.[206,207] The ZrO_2 phase imparted hydrothermal robustness and strong metal anchoring, whereas the TiO_2–WO_x phase offered adjustable Brønsted acidity. The optimized 20 : 8 ratio of Pt/ZrO_2 to TiO_2–WO_x achieved the highest liquid alcohol yield and prolonged stability, exemplifying the principle of modular acid–metal integration for biomass conversion.

Overall, Pt-based catalysts present a versatile platform for selective hydrogenolysis and hydrodeoxygenation, capable of achieving both mild-condition C–C/C–O cleavage and stable long-term operation. Compared with Ru and Pd systems, Pt exhibits stronger C–O activation and greater thermal resilience but typically requires cooperative promoters, such as SnO_x, WO_x, or $Mg(OH)_2$, to balance hydrogenation and acid functions. Rational tuning of Pt dispersion, oxidation state, and support reducibility enables precise control over reaction pathways, directing selectivity between C_2–C_3 diols and C_6 polyols. These insights establish Pt-based materials as key bifunctional catalysts bridging high selectivity with robustness, advancing sustainable catalytic strategies for cellulose-derived platform molecules.

3.3 Non-noble catalysts

Non-noble metal catalysts are increasingly pursued as cost-effective, scalable alternatives to noble metals for aqueous-phase hydrogenolysis of cellulose and its derivatives. Their earth abundance, tunable redox and acid–base chemistries, and intrinsic H_2-activation capability make them attractive for large-scale biomass valorization. Moreover, tungsten-containing oxides and tungstate species have emerged as indispensable promoters, supplying Lewis and Brønsted acidity, oxygen-vacancy redox sites, and strong electronic coupling to transition metal phases. Rather than being treated as an independent class, W-based components are best regarded as cross-cutting modifiers that complement both noble and non-noble hydrogenation centers, establishing bifunctional catalytic ensembles that can orchestrate hydrolysis, RAC, and hydrogenation steps in a concerted fashion. Nevertheless, the practical implementation of non-noble systems faces persistent challenges, including particle sintering, metal leaching, and dependence on soluble acid/base additives, which continue to limit their recyclability and process compatibility. Recent developments have therefore focused on robust bifunctional architectures capable of integrating metallic, acidic, and basic functionalities within stable composite frameworks, allowing selective C–C and C–O bond scission without the need for corrosive cocatalysts.

3.3.1 Transition-metal catalysts. Transition-metal catalysts, mainly Ni-, Cu-, and Co-based systems, together with their alloys, phosphides, and carbides, represent the cornerstone of non-noble hydrogenolysis catalysis. Their appeal stems from the combination of earth abundance, adjustable hydrogenation activity, and tunable acid–base/redox properties. Because these metals alone do not efficiently cleave β-1,4-glycosidic bonds or mediate selective RAC reaction, recent research has focused on bifunctional architectures that integrate metallic, acidic, and basic domains to orchestrate hydrolysis, isomerization, C–C/C–O bond scission, and hydrogenation in a cooperative fashion. The resulting alloyed, promoted, or structurally confined catalysts now provide a versatile non-noble platform rivaling noble-metal systems in both activity and selectivity.

Cellulose hydrogenolysis. Ni remains the primary non-noble metal for hydrogenolysis due to its high intrinsic hydrogenation activity and low cost. Early work established that metallic Ni alone is insufficient for glycosidic hydrolysis or RAC, but appropriately engineered Ni systems can achieve competitive hexitol and polyol yields. High-loading catalysts such as 70 wt% Ni/Ketjen black provided 67% hexitol yield with notable sintering resistance,[208] while Ni/CNF prepared by chemical vapor deposition reached 92% cellulose conversion and 50% sorbitol selectivity.[209] Further studies revealed that an appropriate balance between metallic active sites and acidic functional groups on Ni/CNF is crucial. A 7.5 wt% Ni/CNF catalyst achieved a sorbitol yield of 76% at 93% cellulose conversion.[210] Notably, bare Ni is unable to promote glycosidic hydrolysis or RAC efficiently, necessitating the incorporation of basic or oxophilic promoters. La_2O_3-modified Ni catalysts exemplify this approach. The basic La phase enhances Ni dispersion, stabilizes active sites, and enables sustained conversion, delivering high EG/1,2-PG yields over multiple cycles.[211] Basic ZnO provides similar functionality by promoting glucose–fructose isomerization and thereby directing the pathway toward C_3 products.[212] Sn promoters modulate hydrogenation strength and C–C scission selectivity. Sun *et al.*[84] reported that metallic Sn in 20% Ni/AC favored EG formation (57.6%), whereas SnO promoted 1,2-PG (32.2%). Xiao *et al.*[85] developed 10% Ni–15% Sn/SBA-15, where mixed-valence SnO_x species provided Lewis acid and redox sites, yielding 55.4% EG and 11.8% 1,2-PG at 245 °C and 5 MPa H_2. Phosphide systems (Ni_2P/AC, Ni_2P/SiO_2) introduce additional bifunctionality, improving dispersion and stability under hydrothermal conditions.[213–215]

Cu and Co catalysts provide complementary acid–base and redox environments that allow fine control over isomerization and C–C cleavage. Xiao *et al.*[86] reported that CuCr(4) with $Ca(OH)_2$ achieved 42.6% 1,2-PG and 31.6% EG at 245 °C, 6 MPa H_2, where $Ca(OH)_2$ promoted glucose isomerization and RAC, outperforming other bases due to the optimal ionic radius and charge density of Ca^{2+}.[87,88] Li *et al.*[216] demonstrated that 10% Co/CeO_x produced 55.2% EG and 33.9% 1,2-PG at 245 °C, with

interfacial Co^{n+}–O_x–Ce^{3+} pairs acting as cooperative acid–base sites, suppressing humin formation.

Advanced alloying extends this functionality further. Pang *et al.*[69] achieved full cellulose conversion and 58% hexitol yield with bimetallic Ni–Rh/MC and Ni–Ir/MC. Zhang *et al.*[217] synthesized a cost-effective $Ni_{4.63}Cu_{1.00}Al_{1.82}Fe_{0.79}$ catalyst, achieving 68.07% sorbitol yield under 488 K and 4.0 MPa H_2 for 3.0 h with the assistance of 0.08 wt% H_3PO_4. Zeolite-supported Ni integrates acidity and confinement, enabling hexitol yield of 58.1% over 17% Ni/ZSM-5 (ref. 218) and 76.9% with NiPt/ZSM-5 while preserving stability over cycles.[219] These examples highlight the versatility of transition-metal frameworks for tuning hydrolysis–hydrogenation cooperativity.

Monosaccharides and polyols hydrogenolysis. The hydrogenolysis of glucose and fructose offers a mechanistically simplified platform to probe C–C and C–O activation, avoiding the β-1,4-glycosidic hydrolysis barrier. The reaction proceeds *via* glucose–fructose isomerization, RAC to C_2–C_3 carbonyl intermediates, and hydrogenation to polyols. Non-noble Ni-, Cu-, and Co-based catalysts have provided critical insight into how electronic structure and surface chemistry dictate product selectivity.

Kirali *et al.*[220] prepared Ni–Mo/MC catalysts for converting aqueous glucose, where Ni facilitated the dispersion of Mo and partial reduction of Mo^{6+} to Mo^{4+}/Mo^{5+}, generating Lewis acidic centers that assisted RAC, affording 63.2% EG at 200 °C and 4 MPa H_2. Basic supports such as MgO and ZnO enhance glucose–fructose isomerization, a key upstream step controlling whether C_2 or C_3 pathways dominate, and enable selective formation of 1,2-PG.[221] A weakly basic 10% Co/CeO_x system for fructose conversion achieved a 50.8% yield of 1,2-PG.[216] B_2O_3-modified Cu/Al_2O_3 for glucose hydrogenolysis showed 49.5% 1,2-PG selectivity,[222] while $La_2O_2CO_3$-modified Cu/Al_2O_3 obtained 32% 1,2-PG yield.[223] Xiao *et al.*[86] found that $Ca(OH)_2$ combined with CuCr(4) boosted glucose to 1,2-PG of 52.8% yield, with Ca^{2+} stabilizing cyclic transition states during glucose–fructose isomerization. These studies collectively demonstrate that coupling redox-active promoters (Mo, Cr, Sn) with hydrogenation metals (Ni, Cu) enhances RAC-hydrogenation synergy, while basic supports (MgO, ZnO, CeO_x, $La_2O_2CO_3$) favor isomerization and suppress condensation. Fine-tuning the acid–base environment through B_2O_3 or alkaline additives governs EG *vs.* 1,2-PG selectivity.

Sorbitol hydrogenolysis, as a representative reaction for polyol conversion, proceeds through dehydrogenation to ketose/aldose intermediates, RAC to C_2–C_3 carbonyls, and hydrogenation to EG and 1,2-PG. The sequence requires intimate cooperation among metal, acid, and base sites, making it an instructive platform for evaluating bifunctional non-noble catalysts. Ye *et al.*[224] employed a 20% Ni–0.5% Ce/Al_2O_3 catalyst with $Ca(OH)_2$ promoter, achieving >90% sorbitol conversion and 55–60% diol (EG and 1,2-PG) yield at 240 °C and 7 MPa H_2 over 12 h. Ce enhanced Ni dispersion and introduced moderate basicity, favoring RAC-hydrogenation coupling. Zhou *et al.*[225] prepared ordered mesoporous M–NiCeAl *via* evaporation-induced self-assembly (EISA), affording 58.1% combined diol yield under 220 °C, 6 MPa H_2 with added $Ca(OH)_2$. Zhang *et al.*[54] found that 8% Ni–2% Re/C produced 15.8% EG and 31.0% 1,2-PG at 250 °C in $Ba(OH)_2$ medium, with Re preventing Ni sintering and enhancing selective C–C cleavage.

Zeolite-mediated confinement alters selectivity. Sivasanker *et al.*[226,227] revealed that Ni–NaY selectively converts sorbitol to 1,2-PG, whereas Pt–NaY favors glycerol. Activity trends Ni > Pt > Ru on NaY zeolites, correlating with sorbitol adsorption strength on Ni(111) surfaces that facilitates C–C activation. 6% Ni/FA catalysts using fly-ash supports achieved 65% conversion and 37% 1,2-PG selectivity at 200 °C and 6 MPa H_2 within 12 h,[228] while 2% Ni_2P/AC in aqueous $Ba(OH)_2$ yielded 17% EG and 29% 1,2-PG under 200 °C, 4 MPa H_2, 0.75 h.[229]

To avoid soluble bases, solid-base catalysts have emerged as a major advance. Cu/CaO–Al_2O_3[230] contained dual $Ca_xCu_yAl_zO_p$ (dehydrogenation and isomerization) and $CuAl_2O_4$ (hydrogenation) domains, achieving high diol yields without alkali. 6% Ni–SrHAP–R[231] exploited the alkalinity of Sr-hydroxyapatite nanorods to achieve ≈60% diol selectivity. Ni–MgO catalysts[232] displayed performance correlated with basicity and the active metal sites, and 3 Ni–7 MgO achieved 80.8% total selectivity (EG, 1,2-PG, and glycerol) at 200 °C and 4 MPa H_2. Across Ni–, Cu–, and Co–MgO series,[233] activity decreased as Ni > Co > Cu, emphasizing the role of basicity and metal–support interaction in C–C cleavage control.

Composite oxides and rare-earth promoters further enhance stability and dispersion. Ni/$Mg_{1.29}Al_{0.06}O_{1.38}$ catalysts derived from layered double hydroxides (LDHs) achieved 97% sorbitol conversion with tunable selectivity governed by surface area and alkalinity.[234] Subsequently, the $Ni_{3.6}Mg_{2.4}Al_2(OH)_{16}CO_3$–SF catalyst obtained by changing the preparation method exhibited higher activity and stability in the conversion of sorbitol.[235] Ni/La_2O_3/ZrO_2 systems[236,237] exhibited strong Ni^{2+}–O–La^{3+} interactions improving dispersion and basicity. 10% Ni/10% La_2O_3/ZrO_2 achieved complete sorbitol conversion and >48% polyol yield at 240 °C under 4.0 MPa H_2.[236] Moreover, 10% Ni/5% La_2O_3/ZrO_2 reached 96.8% sorbitol conversion and 74.8% polyol selectivity at 220 °C and 4 MPa H_2.[237] The cooperative tuning of metal–support interactions, intrinsic basicity, and promoter chemistry in these systems demonstrates how non-noble catalysts can effectively orchestrate dehydrogenation, isomerization, and C–C/C–O bond cleavage in aqueous hydrogenolysis, setting the foundation for the tungsten-assisted systems discussed in the following section.

Across cellulose, monosaccharide, and polyol hydrogenolysis, transition-metal catalysts reveal a unifying design philosophy: the catalytic landscape is governed by the interplay between metallic hydrogenation sites and acid–base or redox co-functions that control isomerization and C–C bond cleavage. Nickel-based catalysts serve as the primary platform, yet Cu and Co analogues offer complementary electronic and acid–base environments. Alloying promoter incorporation and structural confinement within oxides or zeolites enable fine control over reactivity and stability. By integrating these cooperative functionalities, non-noble transition-metal systems can rival noble metals in efficiency and selectivity, offering a sustainable foundation for next-generation hydrogenolysis catalysts.

3.3.2 Tungsten-based catalysts. Tungsten-based catalysts play a pivotal role in cellulose hydrogenolysis owing to their unique combination of redox flexibility and acid functionality. The ability of tungsten to cycle between multiple oxidation states ($W^{6+} \leftrightarrow W^{5+} \leftrightarrow W^{4+}$) allows the coexistence of Brønsted and Lewis acid sites, which cooperatively drive cellulose depolymerization, C–C bond scission, and subsequent hydrogenation of intermediates. This dual-function character distinguishes tungsten systems from conventional oxides and underpins their broad utility in transforming polysaccharides into low-molecular-weight polyols and diols.

Cellulose hydrogenolysis. Under aqueous conditions, tungsten species such as WO_x, WC_x, H_2WO_4, and heteropoly acids are partially reduced to hydrogen tungsten bronzes (H_xWO_3), which act as true active intermediates.[42,238] These bronzes generate protons that provide Brønsted acidity for cellulose hydrolysis, while reduced W centers offer Lewis acid sites for C–C bond cleavage. Liu *et al.*[239] confirmed the reversible transformation of $WO_3 \rightarrow H_{0.23}WO_3 \rightarrow H_{0.33}WO_3$, establishing a proton-coupled redox mechanism that accounts for the dynamic heterogeneous-homogeneous nature of tungsten catalysis. Kinetic analyses of tungstic acids[240] identified $H_3O_{40}PW_{12}$ as the most active hydrolysis catalyst, while isotopic-labeling and DFT calculations[241] confirmed that β-position C–C scission proceeds *via* tridentate coordination of sugars to W–O–W bridges, forming glycolaldehyde, glyceraldehyde, and dihydroxyacetone as primary intermediates. These features establish WO_x/H_xWO_3 as redox-active acid frameworks ideally suited for depolymerization and RAC initiation.

Beyond oxides, tungsten carbides (W_2C/WC_x) represent a second, highly effective class of tungsten-based catalysts distinguished by their Pt-like electronic structure, high resistance to hydrothermal leaching, and strong W–C bonding. These properties allow WC_x to maintain reduced W centers and surface oxygen vacancies under reaction conditions, making them powerful platforms for C–C/C–O bond activation. Ni–W carbide systems consistently deliver state-of-the-art EG yields, as shown in Table 3. A (2% Ni–30% W_2C)/AC-973 catalyst achieved complete cellulose conversion and 61% EG yield at 245 °C and 6 MPa H_2.[40] Post-impregnation treatment minimized W_2C sintering, yielding a highly dispersed 10% Ni-(30% W_2C/AC) catalyst with 73% EG yield.[242] Similar strategies extended to raw lignocellulose, where Ni–W_2C/AC achieved 38.5% 1,2-PG from Jerusalem artichoke tuber (JAT)[243] and 75.6% total diols from untreated woody biomass.[244] Mechanistic analyses[245,246] attributed the high EG selectivity to Ni–W_2C interfacial synergy, which facilitated hydrogen spillover and moderated EG adsorption to prevent over-hydrogenolysis. Wu *et al.*[247] synthesized 9% Ni–13.5% W-graphitic carbon (GC850), $WO_x \rightarrow W \rightarrow WC_x$ evolution with increasing temperature and W loading, delivered 69% EG at 230 °C, 5 MPa H_2. Zhang *et al.*[248] dispersed WC_x on mesoporous carbon, reaching 73% EG. The MC support enhances WC_x dispersion and pore transport, maximizing activity.

Beyond carbides, tungsten phosphides (WP) provide strong W–P bonding and enhanced electronic density at W sites, creating redox-active surfaces that cooperate effectively with hydrogenation metals. Zhao *et al.*[249] obtained 46% EG yield using 2% Ni–20% WP/AC at 245 °C, 6 MPa H_2, and 0.5 h, highlighting the synergistic effect between Ni and WP. Tai *et al.*[250] achieved 65% EG yield and excellent recyclability over H_2WO_4–Raney Ni, outperforming $H_4SiW_{12}O_{40}$, $H_3PW_{12}O_{40}$, and WO_3 analogues. Similar WO_3–Raney Ni composites converted JAT to EG with 41.4% yield,[251] demonstrating the adaptability of W-based systems for diverse carbohydrate substrates.

Support architecture critically governs tungsten dispersion, acidity, and metal–acid proximity. Zheng *et al.*[71] found that 5% Ni–15% W/SBA-15 delivered 76.1% EG yield, whereas Cao *et al.*[252] linked strong NiO–WO_3 coupling in 3% Ni–15% WO_3/SBA-15 to the formation of WO_{3-x} species responsible for selective C–C cleavage (70.7% EG). Adjusting the impregnation solution pH controlled dispersion and acidity. The 10% Ni–20% W/SBA-15 sample prepared at pH = 1 achieved 64.9% EG yield.[253] Baek *et al.*[254] correlated polyol selectivity in (Ni, Cu, Fe, Co)/W/SiO_2–Al_2O_3 catalysts with total surface acidity, with Al-rich Ni/W/SiO_2–Al_2O_3 (Al/(Al + Si) = 0.6) showing optimal performance. Silica- and zeolite-based supports enable *in situ* alloying and controlled reduction. For example, the 7 Ni–20 W–ZnO/Beta catalyst achieved 1,2-PG yield of 35.8%,[255] and self-reducing 10% Ni–15% W/MOR yielded 52.3% EG,[256] while 15% Ni–20% W/SiO_2 nanospheres reached 61–63% EG when chelating agents stabilized Ni species and Ni–W alloys.[257–259] Unique meso-structure silica microspheres further enhanced metal loading and mass transfer, yielding 82.2% total diols.[260]

Heteroatom incorporation and additional metallic or metalloid elements further improve activity. Al-doped Ni–W systems, such as 3 Ni–15 WO_3–3 Al-TUD-1,[261] 5% Al–8% Ni–25% W/NaZSM-5,[262] achieved up to 76% and 89% EG yield, respectively, where Al-induced acid sites promoted depolymerization, W^{5+} vacancies acted as Lewis sites for RAC, and Ni completed hydrogenation. Amorphous NiWB/CNTs,[263] Ni–W/MIL-125(Ti),[264] 5 Ni–15 W–15 Cu/$MgAl_2O_4$,[265] 30% Cu–30% WO_x/AC combined with Ni/AC,[266] and NiCu/WO_3[267] further highlight the importance of tuning metal–support interfaces and oxygen vacancy concentrations to control C–C cleavage selectivity.

Despite their outstanding activity, tungsten-based catalysts can deactivate through leaching, sintering, or phase dissolution under hydrothermal conditions. Stabilization strategies address these challenges. Ti–O–W coordination in Ni–W/MIL-125(Ti) prevented tungsten loss and maintained high activity over seven cycles,[264] while 30% Cu–30% WO_x/AC + Ni/AC dual-bed systems minimized coke formation by coupling vacancy generation and glycolaldehyde hydrogenation.[266] Carbon encapsulation has also proven effective—Ni-W@C_{700} achieved 60.1% EG yield with minimal deactivation,[268] and C,N-modified Ni–W/SiO_2@C_xN_y[269] stabilized metal clusters *via* Ni–N–N coordination, imparting excellent hydrothermal durability.

These results establish tungsten-based materials as multifunctional platforms uniting hydrolysis, RAC, and hydrogenation within a single redox-flexible framework. Their reversible formation of protonated bronzes (H_xWO_3) allows dynamic acid modulation, while coupling with hydrogenation metals such as Ni or Cu enhances reduction capability.

Table 3 Non-precious W-based catalytic systems for conversion of cellulose to low-carbon alcohols in aqueous systems

Entry	Catalyst	T (°C)	P (MPa, H_2)	T (h)	Yield (C mol%)	Ref.
1	(2% Ni–30%W_2C)/AC-973	245	6.0	0.5	EG 61.0 1,2-PG 7.6	40
2	10% Ni–(30% W_2C/AC)	245	6.0	0.5	EG 73.0 1,2-PG 8.5	242
3	4% Ni–20% W_2C/AC	245	6.0	1.3	EG 14.1 1,2-PG 38.5	243
4	4% Ni–30% W_2C/AC	235	6.0	4.0	EG 52.7 1,2-PG 11.9 1,2-BG 5.1	244
5	2% Ni–W_2C/AC-973	245	6.0	0.5	EG 61.0 1,2-PG 7.6	245
6	9% Ni–13.5% W–GC_{850}	230	5.0	2.0	EG 69.2	247
7	WC_x/MC	245	6.0	0.5	EG 72.9 1,2-PG 5.1	248
8	2% Ni–20% WP/AC	245	6.0	0.5	EG 46.0	249
9	Raney Ni + H_2WO_4	245	6.0	0.5	EG 65.0	250
10	Raney Ni + WO_3	245	6.0	2.0	EG 37.6 1,2-PG 6.3	251
11	5% Ni–15% W/SBA-15	245	6.0	0.5	EG 76.1 1,2-PG 3.2	71
12	3% Ni–15% WO_3/SBA-15	230	6.0	6.0	EG 70.7	252
13	10% Ni–20% W/SBA-15	245	5.0	2.0	EG 64.9	253
14	Ni/W/SiO_2–Al_2O_3	245	6.0	2.0	EG 23.3 1,2-PG 5.1	254
15	7Ni–20W–ZnO/Beta	245	6.0	0.5	1,2-PG 35.8	255
16	10% Ni–15% W/MOR	240	5.0	2.0	EG 52.3	256
17	15% Ni–20% W/SiO_2	240	5.0	2.0	EG 61.3	257
18	15% Ni–20% W/SiO_2-EEG	240	5.0	2.0	EG 63.3	258
19	15% Ni–20% W/SiO_2–OH	240	5.0	2.0	EG 63.1	259
20	15% W–5% Ni/MSM	245	6.0	2.0	EG 27.9 1,2-PG 13.9	260
21	3% Ni–15% WO_3–3% Al-TUD-1 (zeolite)	230	4.0	1.5	EG 76.0	261
22	5% Al–8% Ni–25% W/NaZSM-5	220	7.0	6.0	EG 89.0	262
23	NiWB/CNTs	250	6.0	2.0	EG 57.7	263
24	Ni–W/MIL-125(Ti)	245	4.0	2.0	EG 68.7 1,2-PG 6.5	264
25	5Ni–15W–15Cu/$MgAl_2O_4$	245	3.0	2.0	EG 52.8	265
26	30% Cu–30% WO_x/AC + Ni/AC	245	4.0	2.0	EG 71.0	266
27	30% Cu–30% WO_x–10% Ni/AC	245	4.0	2.0	EG 58.0	
28	$Ni_6Cu_{1.5}/WO_3$	245	5.5	4.0	EG 58.9	267
29	Ni–W@C_{700}	240	5.0	1.0	EG 60.1	268
30	Ni–W/SiO_2@C_xN_y	240	5.0	2.0	EG 48.3	269

Monosaccharides and polyols hydrogenolysis. Glucose hydrogenolysis provides a direct window into W-mediated RAC chemistry, allowing decoupling of glycosidic hydrolysis from C–C/C–O activation. Tungsten-based catalysts drive this transformation *via* an isomerization–RAC–hydrogenation cascade modulated by W oxidation state and metal coupling. Zhang *et al.*[32] quantified glucose conversion kinetics using AMT, showing that elevated temperature favored glycolaldehyde formation and validated the kinetic model for concentration–time (*C*–*t*) profiles. Ooms *et al.*[270] extended this concept to concentrated feeds, obtaining 66% EG yield over 2% Ni–30% W_2C/AC-973, while fine control of temperature, pressure, and feed rate enhanced overall efficiency.

Support and metal–acid balance strongly influence glucose fragmentation pathways. Ni-WO_3/SBA-15 catalysts with variable W/Ni ratios revealed that higher ratios favored RAC–hydrogenation pathways to EG, while lower ratios promoted direct hydrogenation to sorbitol.[271] The optimized 5% Ni–15% WO_3/SBA-15 catalyst yielded 41.5% EG at 175 °C, 6 MPa H_2, and 1.3 h. The catalytic performance correlated with structure of tungsten compounds and dispersion, following WO_3 < WO_3/SBA-15 < AMT.[272] Liu *et al.*[273] tuned acid–metal cooperation *via* Cu-WO_x/Al_2O_3 catalysts, showing that isolated WO_4 species combined with tetrahedrally coordinated Al generated Lewis acid sites for glucose–fructose isomerization, while Cu sites catalyzed RAC and hydrogenation to yield 55.4% 1,2-PG at 180 °C, 4 MPa H_2. These results show that controlling W local coordination and redox state provides a powerful handle for steering C_2 *vs.* C_3 polyol distributions.

The W-mediated framework extends naturally to polyol hydrogenolysis, where C–C cleavage depends on stabilizing transient aldose/ketose intermediates and accelerating *retro-*

aldol steps. Tungsten's ability to dynamically interconvert Brønsted and Lewis acid sites facilitates rapid dehydrogenation–cleavage sequences. Metals subsequently hydrogenate the carbonyl intermediates, suppressing recombination or humin formation. This cooperative acid–redox–metal functionality enables tungsten catalysts to couple dehydrogenation, β-C–C scission, and hydrogenation with a degree of selectivity unmatched by other non-noble oxides.

Across cellulose, glucose, and polyol hydrogenolysis, tungsten-based catalysts exhibit a unifying mechanistic paradigm rooted in reversible proton-coupled redox chemistry and the coexistence of Brønsted and Lewis acid sites. Collectively, these studies establish that tungsten species—whether present as oxides, carbides, or phosphides—operate as adaptive redox-acid frameworks that synergize with hydrogenation metals to drive highly selective C–C/C–O activation. Through tunable valence states, proton-coupled redox chemistry, and interface engineering, W-based catalysts unify hydrolysis, RAC, and hydrogenation in a single multifunctional platform. Rational control of tungsten dispersion, support architecture, and acid–metal balance defines a powerful design paradigm for efficient, stable, and recyclable systems in cellulose and sugar hydrogenolysis.

3.4 Advanced catalyst architectures

Despite significant progress in noble- and non-noble-metal catalysts, conventional supported systems still face intrinsic limitations in cellulose hydrogenolysis. Metal nanoparticles and acid/base promoters are typically dispersed randomly on oxide or carbon supports, preventing efficient cooperation between hydrolysis, isomerization, C–C/C–O scission, and hydrogenation sites. Under hydrothermal conditions, these catalysts additionally suffer from sintering, leaching, and structural degradation,[274] which hinder sustained activity and precise control of reaction pathways.

To address these constraints, recent research has moved toward advanced catalyst architectures that combine spatial confinement, electronic modulation, and intentionally organized multifunctional sites within well-defined nanostructures. These systems aim to achieve the threefold objective of (i) maximizing proximity and synergy between hydrogenation and acid–base sites, (ii) stabilizing reactive metal species against thermal and chemical degradation, and (iii) selectively channeling reaction intermediates along preferred pathways toward C_2–C_3 diols and low-carbon alcohols. Such designs draw direct inspiration from enzymatic catalysis, wherein confined microenvironments and cooperative active sites orchestrate complex multi-step transformations with high precision and minimal energy dissipation. In the context of biomass valorization, this paradigm has led to the development of diverse nanoscale configurations—including yolk–shell,[127] core–shell,[191,192] mesoporous,[189] and zeolite-confined catalysts[190]—that deliver superior activity, selectivity, and stability compared with conventional supported systems. The following subsections summarize the underlying principles and representative advances of confined catalysts for biomass hydrogenolysis.

3.4.1 Principles of spatial confinement and electronic modulation. Spatial confinement involves embedding or anchoring active metal species within nanostructured environments such as mesoporous channels, hollow cavities, or interlayer galleries.[275] These confined architectures exert both physical constraints and electronic modulation on the active sites, fundamentally altering catalytic performance.[276]

Physical stabilization and size confinement. Confinement physically restricts the mobility and coalescence of nanoparticles, preventing sintering and preserving uniform dispersion even under harsh hydrothermal conditions.[277] The resulting small, well-dispersed particles ensure consistent exposure of active sites and maintain catalytic stability. Since metal particle size strongly influences hydrogenation and hydrogenolysis selectivity, precise control enabled by confinement directly improves catalytic precision.[278]

Electronic environment modulation. Beyond physical stabilization, confinement significantly modifies the electronic state of metal centers through metal–support interactions. For instance, encapsulating Ru or Pt nanoparticles within zeolitic frameworks can lead to electron-enriched metal centers *via* charge donation from the surrounding lattice.[279] Such tuning of electron density facilitates the activation of H_2 and optimizes adsorption of oxygenated intermediates, enhancing C–O and C–C bond hydrogenation steps.[280]

Intermediate enrichment and shape selectivity. The confined nano-spaces can locally enrich reactants and intermediates by concentration or adsorption effects, thereby accelerating reaction kinetics. Moreover, the geometric constraints of pores or cavities induce shape-selective catalysis, preferentially stabilizing intermediates of specific configurations and suppressing undesired side reactions.[281–283] This combination of molecular sieving and intermediate control is particularly advantageous for the selective hydrogenolysis of carbohydrates to low-carbon alcohols.

3.4.2 Spatial integration of multiple active sites. A defining feature of advanced confined catalysts is their ability to spatially integrate multiple active sites—typically metal, acid, and/or base functions—within a single cooperative framework.[284–287] Within these architectures, metallic sites responsible for hydrogenation and acid/base sites responsible for hydrolysis and RAC are co-located at controlled distances. Such nanoscale proximity enables intermediates formed on one site to undergo rapid conversion on an adjacent site without diffusing into the bulk solution, thereby minimizing side reactions and improving carbon efficiency.[288–290]

A representative example is the yolk–shell catalyst Ru/NC@void@MC–SO_3H designed by Yang *et al.*[127] In this architecture, Ru clusters are confined in the inner core, while sulfonic acid groups are grafted on the mesoporous carbon shell (Fig. 5a–c). The hierarchical structure achieved a 38.0% yield of 1,2-PG with a productivity of 342.86 mol h^{-1} $g_{Ru}{}^{-1}$. Hydrolysis occurred on sulfonic acid sites, glucose isomerization and fructose RAC proceeded on Ru–N_x acid–base pairs, and final hydrogenation was catalyzed by metallic Ru, illustrating seamless integration of multi-step reactions within a confined domain.

Liu *et al.*[188] reported a Pd@W/Al–$MSiO_2$ yolk–shell nanosphere (YSNS) catalyst for cellulose hydrogenolysis to EG. The porous shell protected Pd nanoparticles from sintering and leaching, maintaining 48.5% EG selectivity after five cycles. The confined environment also strengthened W–Al synergy. Extra-framework Al enhanced acidity, while W dispersion improved, affording 56.5% EG selectivity at 96.1% cellulose conversion. Further development of Pd@WO_x–$MSiO_2$[191] (Fig. 6) revealed that oxygen vacancies on W^{5+} sites facilitated C–C bond cleavage, while adjacent Pd sites catalyzed hydrogenation, yielding 59.4% EG.

By systematically tuning shell acidity, Pd@Al–$MSiO_2$ catalysts with varying Al content were optimized (Fig. 7).[192] Tetrahedrally coordinated AlO_4 units introduced abundant Lewis acid sites essential for glucose–fructose isomerization. The optimized Pd@Al_3–$MSiO_2$ catalyst achieved 95.4% glucose conversion and 45.2% 1,2-PG yield, confirming that controlled acid–metal proximity governs product distribution. Likewise, Pd@Al–SiO_2 catalysts[189] prepared by a one-pot sol–gel method achieved 59.3% ethanol selectivity and a total carbon yield of >95% under 245 °C and 4.5 MPa H_2 (Fig. 8), with Al incorporation promoting Pd–O–Si(Al) linkages and Pd^0/$Pd^{\delta+}$ bifunctional ensembles for synchronized cascade reactions. The spatial distribution of active sites ensures the sequential exposure of substrates to acid and metal sites, effectively regulating reaction order and suppressing side reactions.

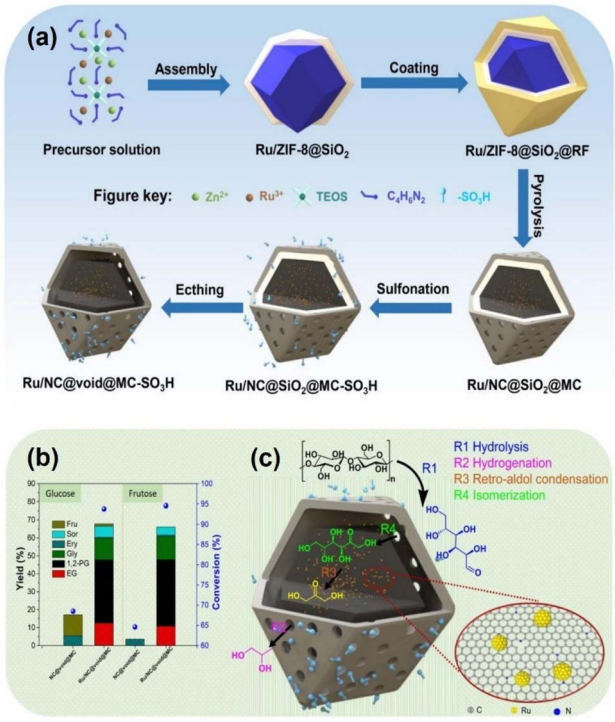

Fig. 5 (a) Preparation process of Ru/NC@void@MC–SO_3H catalyst; (b) performance evaluation of glucose and fructose on NC@void@MC and Ru/NC@void@MC; (c) possible reaction mechanism of cellulose generating 1,2-PG on Ru/NC@void@MC–SO_3H. Reproduced with permission.[127] Copyright 2023, Elsevier.

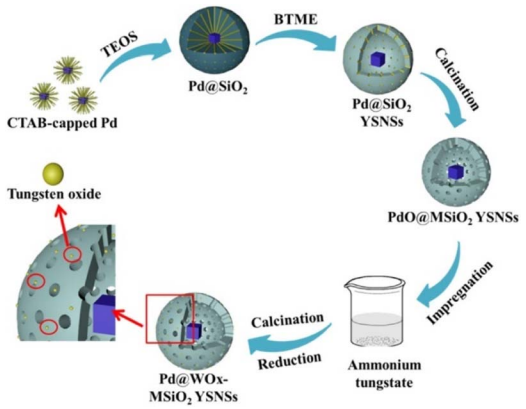

Fig. 6 Schematic representation of the synthesis of Pd@WO_x–$MSiO_2$ YSNSs. Reproduced with permission.[191] Copyright 2021, American Chemical Society.

These results collectively demonstrate that spatial confinement coupled with precisely engineered multi-site integration provides kinetic and thermodynamic control in complex biomass hydrogenolysis pathways.

3.4.3 Zeolite-based confined catalysts. Zeolites constitute a distinctive class of confined catalysts that couple molecular-scale porosity, tunable Brønsted/Lewis acidity, and exceptional hydrothermal stability within crystalline aluminosilicate frameworks. Their ordered micropores not only host metal nanoparticles with high dispersion but also regulate reactant transport and impose shape selectivity, creating an ideal scaffold for constructing multifunctional metal@zeolite catalysts for biomass hydrogenolysis.[281,284] Within these channels, substrates undergo acid-mediated transformations before reaching encapsulated metal centers, thereby enabling spatially synchronized, cascade-type reaction sequences that are difficult to realize on conventional supported catalysts.[275]

The controlled interplay between zeolitic acidity and confined metal centers has been systematically demonstrated by Yu, Xiao, and co-workers, who developed a series of *in situ* encapsulated metal@zeolite catalysts exhibiting enzyme-like cooperativity in hydrogenation and oxidation reactions.[284,287,291] Their studies

Fig. 7 The possible reaction route of glucose hydrogenolysis on Pd@Al–$MSiO_2$ YSNSs. Reproduced with permission.[192] Copyright 2020, Elsevier.

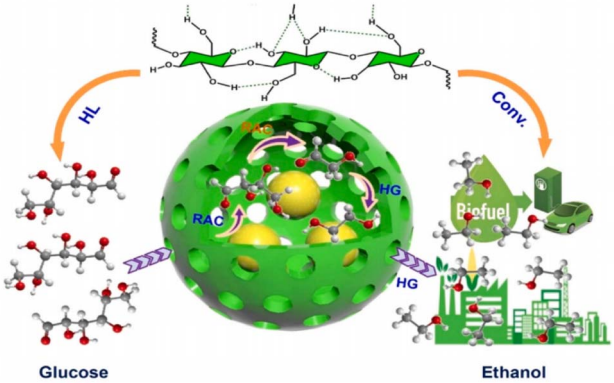

Fig. 8 Schematic representation of cascade steps and active site locations of cellulose hydrogenation to ethanol over Pd@Al_3–SiO_2 catalyst. Reproduced with permission.[189] Copyright 2025, Elsevier.

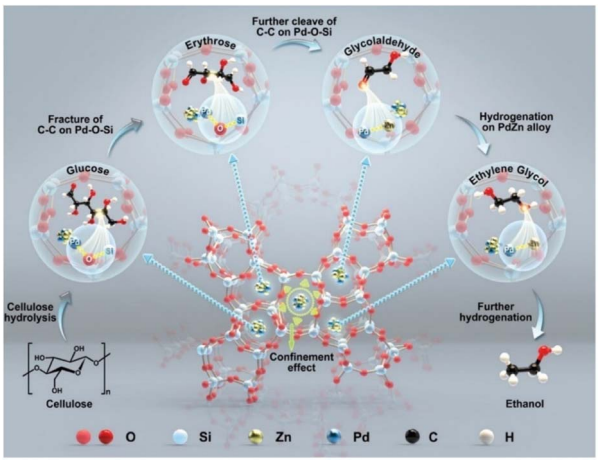

Fig. 9 Presumptive reaction mechanism for the cellulose hydrogenolysis to ethanol over $PdZn_{0.5}$@S-1 catalyst. Reproduced with permission.[190] Copyright 2025, Wiley-VCH.

revealed that the co-confined Brønsted and Lewis sites create a microenvironment capable of orchestrating multistep transformations with high precision.[292] For example, Weckhuysen *et al.* encapsulated ~1 nm Ru clusters within La-modified Y zeolite,[293] the restricted proximity between Ru and acid sites enabled solvent-free conversion of ethyl levulinate to valerate biofuels. Similarly, Cho *et al.*[294] reported a "nest effect" in Pt@H-ZSM-5, where Brønsted acid–metal cooperation facilitated a five-step cascade from furfural to valeric acid and ethyl valerate. These studies collectively highlight how zeolite confinement strategies can orchestrate complex multi-step transformations with high efficiency and selectivity.

The catalytic performance of metal@zeolite systems is governed by their acid–metal balance and nanoscale spatial distribution.[278] In Ru/H-ZSM-5-catalyzed hydrodeoxygenation of levulinic acid, dominant hydrogenation yields γ-valerolactone, whereas stronger acidity drives further conversion to valeric acid.[58] Rational tuning of acid–metal ratios during synthesis thus becomes essential for optimizing selectivity. Moreover, as emphasized by de Jongh and other researchers,[288–290] nanoscale site separation governs electronic coupling between metal and acid centers, which in turn tunes adsorption and activation energies.[280]

Building on these principles, our group designed Pd_xZn_y@S-1 zeolite catalysts *via* a ligand-protection and direct hydrogen-reduction strategy.[190] The PdZn alloy clusters and adjacent $Pd^{\delta+}$–O(H)–Si coordination within the S-1 zeolite respectively act as hydrogenation and acid sites, forming bifunctional active sites that significantly enhanced the hydrogenolysis of cellulose to ethanol (Fig. 9). This architecture modulated Pd's electronic structure and acid density, achieving 69.2% ethanol selectivity and 97.4% total carbon yield from cellulose, and surpassing most reported heterogeneous systems.

Across yolk–shell, core–shell, mesoporous, and zeolite-confined catalysts, three unifying principles emerge: (i) nanoscale confinement prevents sintering, maintains metal dispersion, and enables size-dependent selectivity; (ii) electronic coupling between confined metals and supports tailors adsorption and activation energies for optimized hydrogenation and C–C cleavage; and (iii) spatial integration of multifunctional sites minimizes diffusion losses and promotes synchronized cascade reactions. These spatially engineered architectures establish a robust and sustainable platform for the selective conversion of lignocellulosic biomass into low-carbon alcohols and other renewable chemicals, bridging fundamental catalytic principles with practical, high-efficiency biomass valorization.

In summary, although the aforementioned advanced architectures exhibit material diversity, their design adheres to transferable universal principles. Spatial confinement, as a physical stabilization strategy, can effectively prevent the sintering and leaching of various active components under hydrothermal conditions. Electronic modulation, achieved through well-designed metal–support interfacial interactions, provides a general means to regulate the electron density of different active centers and optimize their adsorption and activation behaviors toward reactants. The nanoscale integration of multiple active sites serves as a universal blueprint for constructing efficient tandem catalytic reactions. Its core lies in the precise control of distances between acid, base, and metal sites to ensure the directed and rapid transfer of intermediates. Together, these principles form the architectural foundation for the rational design of high-performance cellulose hydrogenolysis catalysts that transcend specific materials.

Although remarkable progress has been made, key challenges remain in quantitatively correlating site proximity (*e.g.*, optimal site spacing and acid/metal ratio windows) with turnover-determining steps, understanding dynamic restructuring under hydrothermal conditions, and scaling deterministic confinement. Future progress will rely on operando spectroscopy, microkinetic modeling, and adaptive supports capable of on-demand tuning of metal–acid interactions.

4 Product-oriented pathways and selectivity principles

The catalytic conversion of cellulose into well-defined alcohols represents a critical step toward the sustainable utilization of

lignocellulosic biomass. While mechanistic studies elucidate how individual bond-breaking and hydrogenation steps proceed, and catalyst design focuses on optimizing active-site structures, product-oriented strategies integrate both dimensions—linking reaction pathways to the architecture and electronic properties of the catalyst.

Selectivity in hydrogenolysis arises not from a single active function but from the cooperative synchronization of acid, base, and metal sites that govern hydrolysis, isomerization, C–C/C–O bond cleavage, and hydrogenation in sequence. The distribution of products, ranging from C_2 (EG, ethanol) to C_3 (1,2-PG) and C_6 (polyols), is determined by how these functions interact dynamically within the catalytic microenvironment. Building upon the mechanistic insights outlined in Section 2 and the catalyst architectures described in Section 3, this chapter examines how the interplay between electronic structure, acid–base balance, and spatial organization directs selectivity toward specific products, using ethanol, EG, 1,2-PG, and polyols as representative cases.

4.1 Ethanol system

Ethanol, a key platform molecule for both renewable fuels and fine chemicals,[295] serves as a benchmark for C_2-selective hydrogenolysis. Its formation from cellulose proceeds through sequential hydrolysis, RAC, and hydrogenolysis steps, where C–O bond cleavage and subsequent hydrogenation of C_2 intermediates define the selectivity window. Achieving high ethanol yields requires precise coordination of acid and metal functionalities to steer the reaction toward C_2 termination rather than over-fragmentation or polymerization.

As shown in Table 4, tungsten-containing catalysts have emerged as the most effective systems for ethanol-oriented hydrogenolysis. In Mo/Pt/WO_x catalysts, interfacial O_xMo–Pt–WO_x ensembles promote C–O bond scission in EG intermediates, achieving 43.2% ethanol selectivity under hydrothermal conditions.[26] Similarly, Pd–Cu–WO_x/SiO_2 catalysts enable one-pot cellulose conversion to ethanol with over 42% yield, benefiting from cooperative effects between redox-active WO_x and bimetallic hydrogenation centers.[27] In both systems, dynamic electron transfer between metal and oxide components stabilizes W^{5+} species and generates acid sites *in situ*, facilitating selective C–O cleavage without over-hydrogenation.

Protonic acid–metal composite systems provide an alternative route for ethanol synthesis. In H_2WO_4–Pt/ZrO_2 catalysts, the balanced Pt^0/Pt^{2+} ratio ensures controlled hydrogenation of C_2 intermediates, while H_2WO_4 selectively cleaves C–C bonds in glucose, directing carbon flux toward ethanol.[28] Other studies have demonstrated similar synergy in combined Ni@C–H_3PO_4 systems, where protonic acids accelerate hydrolysis and retro-aldol steps, and metal sites facilitate hydrogenation.[29] The key lies in maintaining an intermediate acidity level that enhances depolymerization and C–C scission while preventing dehydration or carbon loss.

Recent progress in spatially confined hybrid catalysts has further advanced ethanol selectivity. Fu *et al.*[95] developed the Ru-WO_x/HZSM-5 and obtained an ethanol yield of 42.3% after 24 h of reaction. The highly dispersed Ru_3W_{17} alloy had a moderate acid site and showed a synergistic catalytic effect with HZSM-5. Hollow Pt@HZSM-5 (ref. 30) and Pd@Al–SiO_2[189] catalysts integrate acid and metal functions within nano-confined architectures, promoting tandem hydrolysis–hydrogenation reactions while minimizing diffusion loss of intermediates. The PdZn@S-1 zeolite system exemplifies this principle. The "restricted adjacency" between PdZn alloy sites and nearby Pd–O(H)–Si groups forms bifunctional ensembles of hydrogenation and Lewis-acid centers, achieving 69.2% ethanol selectivity and nearly complete carbon recovery.[190]

These results collectively reveal that ethanol selectivity is dictated by C–O bond activation preference and the stability of C_2 intermediates, both governed by acid–metal synergy and local electronic structure. Rational control over metal–oxide interfaces and confinement thus enables the programmable conversion of cellulose into ethanol with molecular-level precision.

4.2 EG system

Among the various polyols derived from cellulose hydrogenolysis, EG occupies a uniquely central position due to its high carbon efficiency, chemical stability, and broad industrial relevance as an antifreeze, solvent, and polymer precursor. From a mechanistic standpoint, EG formation represents a selectivity-controlled termination point within the C_2–C_3 scission network, specifically, the selective hydrogenation of glycolaldehyde intermediates derived from glucose RAC. Thus, understanding EG selectivity requires analyzing how catalyst architecture regulates β-C–C bond cleavage, intermediate stabilization, and hydrogenation kinetics within a single catalytic framework.

Tungsten-based catalysts uniquely fulfill these requirements through redox-active acid–metal cooperation. Under hydrothermal conditions, WO_3 species are partially reduced to hydrogen tungsten bronzes (H_xWO_3),[42] which generate both Brønsted and Lewis acid sites. The variable valence of tungsten enables reversible redox cycling ($W^{6+} \leftrightarrow W^{5+}$), maintaining continuous activity for C–C scission and hydrogenation.[238–240] In Ni–W_2C, Ni–WO_3/SBA-15, and Ni–W/MOR systems, strong electronic coupling between Ni and W centers enhances hydrogen spillover and moderates EG adsorption, suppressing over-hydrogenolysis. Optimized catalysts achieve EG selectivities exceeding 70% under 230–245 °C and 3–6 MPa H_2, with stable performance across multiple cycles.[40,71,256]

The metal–support interface plays an equally decisive role. Supports such as SBA-15, SiO_2, or ZnO[254,257] adjust surface acidity and confine intermediates within mesoporous environments, preventing excessive fragmentation. The acidity-reducibility balance of the support defines how long reactive intermediates reside near the metal–oxide interface, directly shaping selectivity. When WO_{3-x} domains remain partially reduced, β-C–C cleavage to glycolaldehyde is favored;[252] excessive reduction to W_2C or WC drives deeper fragmentation toward methanol or methane.[247] Metals such as Ni and Ru maintain the optimal W^{5+}/W^{6+} ratio, while Cu or Al modifiers introduce weak basicity that further suppresses over-cleavage.[261–263]

Table 4 Different catalytic systems for the conversion of cellulose to ethanol

Catalyst	Solvent	T (°C)	P (MPa)	T (h)	Yield (C mol%)	Ref.
Ni–W + Cu/SiO_2	Tetrahydrofuran	280	$3.0H_2$	—	29.0	296
Pt–Cu/SiO_2	Tetrahydrofuran	230	$3.0H_2$	—	44.0	297
$Mo/Pt/WO_x$	H_2O	245	$6.0H_2$	2.0	43.2	26
Pd–Cu–WO_x/SiO_2	H_2O	300	$4.0H_2$	10.0	42.5	27
H_2WO_4 + Pt/ZrO_2	H_2O	250	$4.0H_2$	5.0	32.0	28
H_3PO_4 + Ni@C-700	H_2O	200	$5.5H_2$	3.0	69.1	29
5Ru–$25WO_x$/HZSM-5	H_2O	235	$3.0H_2$	24.0	42.3	95
Pt/WO_x + Pt@HZSM-5	H_2O	245	$4.0H_2$	4.0	54.4	30
Pd/Fe_3O_4	H_2O	240	$0.5N_2$	12.0	51.0	183
Pd@Al–SiO_2	H_2O	245	$4.5H_2$	4.0	59.3	189
PdZn@silicalite-1	H_2O	245	$4.5H_2$	4.0	69.2	190

Spatial confinement offers an additional level of selectivity control. Encapsulated nanoreactors, such as core–shell Ru@acid-functionalized oxides, enable hydrolysis near the shell and RAC-hydrogenation near the core, allowing diffusion-mediated regulation of product ratios.[127] In temperature-responsive H_2WO_4 systems, partial dissolution under reaction conditions followed by reprecipitation upon cooling provides a self-regulating supply of active species, ensuring stable W valence distribution.[114]

Overall, EG formation exemplifies the threefold coordination of catalytic functions: redox-active tungsten oxides provide dynamic acidity, metallic centers control hydrogenation selectivity, and structured supports define the microenvironment for intermediate stabilization. Together, these factors allow EG production to be directed by rational design rather than empirical optimization.

4.3 1,2-PG system

The selective formation of 1,2-PG illustrates how subtle tuning of acid–base and metal functions directs the reaction pathway toward C_3 products. While EG arises from β-C–C bond cleavage in glucose, 1,2-PG originates from glucose–fructose isomerization followed by γ-C–C bond scission through RAC of fructose to dihydroxyacetone and glyceraldehyde, which are then hydrogenated into 1,2-PG. Selectivity thus depends on synchronizing these sequential reactions—each requiring distinct catalytic functions.

Lewis acid-mediated isomerization initiates this transformation by rearranging glucose to fructose through 1,2-hydride shifts. Catalysts containing W^{5+}, Al^{3+}, or Sn^{4+} centers (in WO_x, Al_2O_3, Sn-Beta, Sn-MFI) generate coordinatively unsaturated Lewis acid sites that polarize the carbonyl group and enable hydride migration or a ring-opening-ring-closure mechanism of the pyranose form to facilitate glucose–fructose isomerization.[298–301] These same centers subsequently promote RAC to form C_3 intermediates, while adjacent metallic sites (Ni, Cu, Pd, or Pt) hydrogenate them to 1,2-PG. The acid–metal balance determines product distribution. Excessive acidity accelerates cleavage to C_2 species, while insufficient acidity hinders isomerization. Systems such as Pd–WO_x/Al_2O_3,[302] Cu–WO_x/Al_2O_3,[273] and CuB/Al_2O_3[222] achieve an optimal middle ground, producing 45–56% 1,2-PG from glucose with minimal over-fragmentation.

Basic co-catalysts introduce a complementary control dimension. Moderately basic supports such as MgO,[221] ZnO,[212] or $La_2O_2CO_3$[223] promote enediol formation *via* proton abstraction at C_2, lowering the barrier for glucose–fructose isomerization. The ionic radius and basicity of these oxides modulate intermediate stability and suppress humin condensation.[223] When coupled with metal sites, such as in CuCr–$Ca(OH)_2$ (ref. 86 and 87) or Ni–W–ZnO, Ni–MgO–ZnO[212,255] systems, the proximity of base and metal centers ensures rapid turnover between isomerization, RAC, and hydrogenation, producing 1,2-PG yields up to 53% under hydrothermal conditions.

Tin-based systems represent a particularly versatile platform because Sn species provide both Lewis acidity and redox flexibility. Framework-incorporated Sn^{4+} sites in Sn-Beta or Sn-MFI zeolites act as solid Lewis-acid analogues of enzymes, catalyzing glucose isomerization and RAC with water-tolerant stability.[82,89,90] Surface SnO_x species further tune adjacent metal electronic states, steering the EG/1,2-PG ratio.[84] The Sn/metal ratio and Sn valence state control this bifunctional synergy: low Sn loading favors hydrogenation-dominant PtSn alloys, while higher Sn content enhances Lewis acidity and directs selectivity toward 1,2-PG.[83] Redox cycling between Sn^{2+} and Sn^{4+} dynamically adjusts oxygen-vacancy concentration, stabilizing intermediates and avoiding over-hydrogenation.[85] These tunable Sn-metal ensembles thus offer a "programmable" route to C_3 diols, achieving 25–35% 1,2-PG selectivity with compositional control in representative catalysts such as 5% Ru–3% Sn/AC[156] and Ni–SnO_x/SBA-15.[85]

In essence, the 1,2-PG system demonstrates how acid–base-metal cooperation and site proximity orchestrate selective cascade catalysis. Lewis acids enable molecular rearrangement, bases stabilize reactive intermediates, and metals initiate hydrogenation precisely at the C_3 stage. Through architectural design, reaction networks once governed by competition among pathways become programmable at the molecular scale.

4.4 Polyol system

Polyols such as sorbitol and mannitol represent the high-carbon branch of cellulose hydrogenolysis, where the carbon skeleton of glucose is preserved rather than cleaved. Their selective formation depends on the kinetic synchronization between cellulose depolymerization and glucose

hydrogenation.[303] Acidic sites catalyze the hydrolysis of β-1,4-glycosidic bonds, while metal sites hydrogenate the resulting glucose into polyols. If these steps are not properly balanced, intermediates undergo side dehydration or condensation, leading to humins or gaseous byproducts. Hence, controlling the relative rates of hydrolysis and hydrogenation is the decisive factor for polyol selectivity.

Nickel-based systems remain the most studied non-noble catalysts for polyol formation, combining strong H_2 activation[304–306] with cost-effectiveness. Ni-rich catalysts benefit from the high H-dissociation capacity of $Ni^0/Ni^{\delta+}$, but suffer from sintering, leaching, and excessive hydrogenolysis under hydrothermal conditions.[307–309] Electronic modulation *via* P or trace Rh, Ir, Pt to form Ni_2P[213–215] or Ni–M alloys[69] weakens Ni–H bonding and geometrically isolates Ni, raising sorbitol selectivity from ∼40% to >60%. Supports such as CNF,[209] MC[208] and ZSM-5 (refs. 56 and 218) with low Brønsted acidity and high surface area supply mild hydrolysis sites and anchor Ni through defects or N/O functions, securing high dispersion at minimal acid density. The hydrogenation depth is governed by electron transfer between Ni and the promoter, while surface chemistry of the support controls Ni stability; only their concerted optimization delivers cost-effective, durable Ni catalysts.

Noble metal systems are predominantly based on Ru catalysts. Ru catalysts exhibit 1–2 orders of magnitude higher hydrogenation activity than Ni,[309,310] enabling operation under mild conditions that suppress sugar degradation. acid–metal nano-pairing—nanoscale contact of Ru with mineral or heteropoly acids—drives cellulose hydrolysis to glucose and immediate hydrogenation to sorbitol, curbing inhibitor accumulation.[116,164] Optimal acid strength and 2–3 nm Ru particles are required to avoid side reactions and over-hydrogenolysis.[122,124] Functionalized supports (CNT,[136] N-doped carbon,[137,138] sulfonated carbon,[104–107] niobium phosphate,[109] zeolites[110,111]) stabilize Ru and promote hydrogen spillover, mitigating leaching and oligomer deposition. Systems such as HPA–Ru/C,[121,125,126] Ru/CNT,[123,134,146–148] Ru–N/C,[139] and Ru/$NbOPO_4$ (ref. 109) deliver 70–90% sorbitol yield at >80% selectivity for ≥4 cycles with <3 wt% Ru, decoupling high activity from stability and offsetting noble-metal cost.

Across ethanol, EG, 1,2-PG, and polyol systems, the formation of specific products in cellulose hydrogenolysis is determined by how acid, base, and metal functionalities are balanced and spatially coordinated. Acid strength dictates whether C–O or C–C bonds are cleaved first; the metal phase governs the depth of hydrogenation; and the surrounding framework defines how intermediates migrate and transform. Product selectivity thus emerges from a kinetic and structural hierarchy rather than from any single component. Three factors recur throughout all systems. First, interfacial electronic structure, especially charge transfer at metal–oxide or metal-phosphate boundaries, controls the activation barriers of key elementary steps such as glucose isomerization, RAC, and C–O hydrogenolysis. Second, acid–base balance tunes the ratio of β- to γ-C–C cleavage, guiding carbon flow between C_2 (EG and ethanol), C_3 (1,2-PG), and C_6 (polyol) products. Third, spatial confinement and site proximity enable consecutive reactions to proceed in one domain, preventing undesired condensation and improving carbon efficiency.

Together, these principles define a unified mechanistic logic for product-oriented catalyst design. By integrating acid, metal, and structural functions within a coherent architecture, it becomes possible to steer the cellulose hydrogenolysis network toward predetermined molecular outcomes with both high selectivity and operational stability—a necessary foundation for scalable, sustainable biomass valorization. However, achieving high selectivity under laboratory conditions does not necessarily guarantee process viability. The formation and transformation of these target molecules are strongly influenced by reactor environment, mass and heat transfer, and feedstock heterogeneity, all of which evolve dramatically when moving from gram-scale experiments to continuous industrial operation. To translate these molecular-level insights into scalable technologies, the focus must shift from active-site design to the engineering of entire catalytic processes. Reactor configuration, flow regime, substrate feeding strategy, and pretreatment protocols collectively determine whether catalytic pathways established in fundamental studies can be realized at the process level. Consequently, Section 5 integrates these aspects into a unified engineering framework, linking intrinsic catalytic kinetics with reactor hydrodynamics, feedstock preparation, and industrial-scale implementation.

5 Reaction engineering and process perspectives

The catalytic hydrogenolysis of cellulose to low-carbon alcohols is a quintessential multiscale reaction system, involving molecular transformations at the catalyst surface and collective phenomena in multiphase flow environments. Achieving practical efficiency and selectivity requires uniting molecular-level design with reactor- and process-level optimization. This section thus focuses on the engineering dimensions of biomass hydrogenolysis, highlighting how reaction configuration, feedstock preparation, and process intensification translate catalytic principles into sustainable industrial practice.

5.1 Reactor modes and operations

Hydrogenolysis of cellulose proceeds through sequential hydrolysis, RAC, and hydrogenation. The spatial–temporal coupling of these steps is profoundly influenced by reactor configuration and operational parameters.

Batch reactors remain indispensable tools for intrinsic kinetic analysis and mechanistic elucidation. They allow precise temperature and pressure control and provide valuable information on activation energies for cellulose hydrolysis (120–180 kJ mol^{-1}),[70] glucose RAC (≈145 kJ mol^{-1}),[32] and hydrogenation (<50 kJ mol^{-1}).[31] Temperatures exceeding 453 K represent a critical threshold for the cleavage of β-1,4-glycosidic bonds[24,25,69] and the rate of RAC.[71,114] However, the batch reactors' closed nature promotes intermediate accumulation, leading to secondary condensation, humin formation, and a rapid decline in EG selectivity.[62,63] Thus, batch operation

serves primarily as a diagnostic tool for understanding elementary kinetics rather than for optimizing selectivity.

Semi-continuous reactors bridge kinetic studies and process-level optimization. Continuous substrate feeding at differential rates (typically ~2 mL min^{-1} for glucose solutions) maintains a low steady-state concentration of reactive intermediates, reducing the rate of polymerization and enhancing EG selectivity from ~17% to >50%.[33] This "differential substrate input, cumulative product output" principle underpins most kinetic models that describe tandem hydrolysis–hydrogenation systems.

Continuous-flow reactors mark the transition from experimental demonstration to industrial application.[311] They ensure steady-state conditions, minimize heat and mass-transfer gradients, and enable real-time control of residence time distribution (RTD). Two major strategies dominate: (i) direct solid feeding, wherein wet or dry cellulose slurries (10–28 wt%) are introduced by screw or piston pumps into pressurized stirred reactors, yielding 40–65% EG at high throughput;[51,67] and (ii) two-step saccharification–hydrogenation, where cellulose is pre-hydrolyzed to soluble oligosaccharides before hydrogenation, doubling total diol yield relative to untreated cellulose.[68]

Emerging reactor concepts, including structured catalytic membranes, microchannel reactors, and slurry-fixed hybrid beds, seek to minimize external mass-transfer resistance while maximizing interfacial contact. These designs also facilitate continuous catalyst regeneration and heat recovery, aligning process intensification with catalyst durability.

5.2 Feedstock and pretreatment

In practical operation, catalytic hydrogenolysis must address the complexity of real lignocellulosic biomass rather than purified cellulose powders. Native biomass contains cellulose fibrils embedded within a matrix of hemicellulose, lignin, extractives, and inorganic minerals.[17,312] These non-cellulosic components strongly influence catalyst accessibility, reaction selectivity, and stability, and therefore pretreatment becomes essential for achieving reproducible, high-yield production of low-carbon alcohols.

Among all structural components, lignin is the most detrimental to hydrogenolysis performance. Studies using Ni–W_2C/AC systems revealed a clear negative correlation between EG yield and lignin content despite nearly complete biomass conversion (Fig. 10).[34] Aromatic fragments derived from lignin depolymerization tend to adsorb irreversibly on metallic sites, suppressing hydrogenation and promoting humin formation.[244] By contrast, hemicellulose frequently exerts a beneficial effect, as its hydrolysis products include C_2–C_3 fragments that can be further converted to EG and 1,2-PG, thereby increasing overall carbon efficiency.

Another major challenge arises from inorganic ions, especially Ca^{2+}, Mg^{2+}, and Fe^{3+}, which readily precipitate as inactive tungstates (*e.g.*, $CaWO_4$, $Fe_2(WO_4)_3$) under hydrogenolysis conditions, irreversibly deactivating W-based catalysts.[313] Systematic work on poplar, pine, corn stover, miscanthus, and other feedstocks indicates that maintaining divalent-cation concentrations below ~4 mmol kg^{-1} is necessary to preserve catalytic activity and avoid batch-to-batch variation.[314]

Pretreatment strategies therefore focus on removing lignin and mineral contaminants, opening up the plant cell wall, and exposing cellulose fibrils to catalytic hydrolysis and hydrogenation.[34] Alkaline delignification (*e.g.*, ammonia or NaOH) effectively disrupts lignin–carbohydrate complexes, swells cellulose fibers, and enhances hydrolytic accessibility. When combined with mild oxidative steps (*e.g.*, H_2O_2 treatment), the combined EG and 1,2-PG yield can increase to 48%. Crucially, acid washing following alkaline pretreatment removes residual Ca^{2+}/Fe^{3+} ions and prevents the formation of inactive tungstate phases, reinstating high catalytic activity and ensuring stable long-term operation.[315] These principles hold across a wide spectrum of herbaceous feedstocks, enabling combined diol yields above 50% even at high solid loadings.[67,260]

Beyond chemical delignification, mechanical activation—including ball milling and steam explosion—partially amorphizes cellulose, lowers crystallinity, and improves wetting and catalyst–substrate contact. Enhanced accessibility yields consistently higher EG production across agricultural residues such as corn cob, wheat straw, and bamboo, and reduces mass-transfer limitations in continuous-flow reactors where solid–liquid contact becomes rate-limiting.[257] Mechanical–chemical synergy is thus emerging as a practical approach for improving both selectivity and throughput.

Woody biomass presents a contrasting but equally important scenario. Although more recalcitrant due to its dense fiber architecture, wood typically contains fewer soluble minerals and can be rendered compatible with tungsten-based or noble-metal catalysts through combined mechanical activation and mild acid-assisted delignification. Using Ni–W_2C catalysts, birch and pine have been converted into EG and 1,2-PG with total yields of 45–75% (based on sugars), while lignin is simultaneously depolymerized into monophenols with yields around 40–50%.[244] Noble-metal catalysts such as Ru/C or Pt/C can also efficiently upgrade pretreated wood, achieving ~55–62% yields of C_4–C_6 sugar alcohols after mechanical activation or acid-assisted pretreatment.[116,316] These examples highlight how targeted disruption of woody tissue architecture enables its effective incorporation into hydrogenolysis processes.

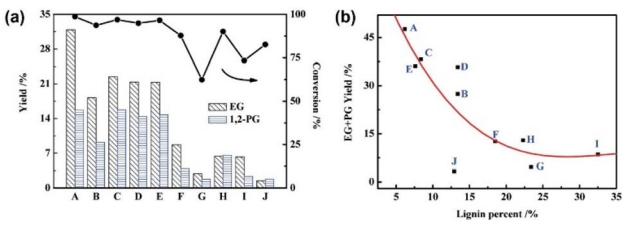

Fig. 10 (a) Catalytic performance of corn stalk after various pretreatments. (b) Plot of overall yields of EG and 1,2-PG as functions of lignin percent in corn stalks. (A) Ammonia and H_2O_2, (B) butanediol, (C) NaOH, (D) H_2O_2, (E) ammonia, (F) 50% ethanol, (G) hot water, (H) hot limewater, (I) SC-CO_2, (J) raw corn stalk (Reaction conditions: 2% Ni–30% W_2C/AC, 245 °C, 2.5 h). Reproduced with permission.[34] Copyright 2011, American Chemical Society.

Looking beyond conventional acid–base routes, organic-solvent fractionation has recently emerged as a low-energy pretreatment option capable of simultaneously deconstructing biomass and stabilizing lignin fragments. Ethanol–water mixtures partially delignify straw and produce clean carbohydrate streams suitable for Ru–W catalysis,[317] while formaldehyde-assisted acidic solvents enable near-complete fractionation of cellulose, hemicellulose, and lignin with 76–90% efficiency.[318] Importantly, formaldehyde prevents lignin recondensation and generates stable, valorisable aromatic intermediates—offering promising integration with biorefinery operations.

It should be noted that efficient chemical pretreatment methods (such as acid–base treatment and organic solvent fractionation), while effectively removing lignin, may introduce soluble impurities (*e.g.*, residual alkaline agents, inorganic salt ions, or organic solvent molecules). If these impurities are not effectively removed, they will enter the subsequent hydrogenolysis reactor along with the cellulose-rich stream. This can potentially poison the acid/base or metal sites of the catalyst or alter the reaction microenvironment, thereby affecting catalytic activity and product selectivity. Therefore, developing supporting purification steps (such as thorough washing and solvent recovery) or designing pretreatment-catalysis integrated processes compatible with downstream catalytic systems is a crucial link in achieving efficient and stable biomass refining.

Overall, feedstock composition and pretreatment fundamentally determine the kinetics, selectivity, and durability of catalytic hydrogenolysis. Removing lignin, extractives, and mineral ions enhances cellulose accessibility, suppresses catalyst poisoning, and stabilizes active sites—effects that are especially critical under high-solid, continuous-flow conditions. The convergence of mechanical activation, mild chemical delignification, and energy-efficient solvent fractionation defines a new generation of integrated pretreatment strategies capable of converting diverse lignocellulosic biomass into uniform, catalyst-ready intermediates. Such advances will be essential for scaling the continuous production of bio-based low-carbon alcohols.

5.3 Industrial and techno-economic outlook

The industrial realization of bio-based low-carbon alcohols, particularly EG, requires the coordinated optimization of feedstock processing, catalytic system design, reactor operation, and product purification. Moving from laboratory studies to scalable production demands simultaneous advances in feedstock utilization, catalyst durability, process intensification, and energy-efficient separation.

A central determinant of commercial viability is feedstock pretreatment, which governs both catalyst accessibility and long-term stability. Green and cost-effective methods such as dilute acid or alkali pretreatment, ammonia fiber expansion, and steam explosion effectively remove lignin and disrupt cellulose crystallinity, improving EG yields while prolonging catalyst lifetime. Sustainable biomass supply chains, optimized within short collection radii, are equally important to reduce logistics costs and carbon footprints. Operationally, moderate hydrogen pressures (3–6 MPa) and temperatures (230–270 °C) strike a balance between conversion and energy consumption; overly harsh conditions accelerate humin formation and catalyst deactivation, while mild conditions supported by bifunctional catalysts sustain continuous, high-selectivity conversion.[43]

Catalyst stability remains the dominant cost factor in techno-economic analyses. Tungsten-based species such as tungstic acid and WO_3 show excellent recyclability through precipitation–calcination or residue distillation after EG recovery. For hydrogenation, skeletal or supported Ni catalysts (*e.g.*, Raney Ni, Ni–P, Ni–Mo alloys) exhibit strong hydrothermal stability and mechanical robustness.[319] Nevertheless, lignin-derived aromatics can poison active sites and suppress hydrogenation;[244] periodic solvent-assisted regeneration or mild oxidative cleaning is therefore essential. Alloying, phosphidation, or core–shell encapsulation strategies further enhance hydrothermal endurance without sacrificing selectivity.

In large-scale and continuous biomass conversion systems, catalyst deactivation primarily stems from chemical poisoning/blockage (*e.g.*, adsorption of lignin-derived aromatics and humins), leaching of active components (hydrothermal dissolution), and structural sintering. The aforementioned strategies, such as alloying, phosphidation, and core–shell encapsulation, represent proactive designs targeting these failure modes: core–shell structures physically confine and inhibit the sintering and leaching of active components; alloying and phosphidation modulate the surface electronic structure to weaken the strong adsorption of oxygenated intermediates or coke precursors, thereby enhancing anti-coking capability; carrier surface engineering (*e.g.*, hydrophilicity/hydrophobicity tuning) helps reduce the retention of large-molecular-weight by-products. Consequently, the long-term stability of catalysts requires synergistic design encompassing intrinsic material properties, microstructure, and surface/interface characteristics.

Large-scale production depends on process intensification and continuous operation. Plants exceeding 100 000 ton per yearmust employ continuous or semi-continuous reactors to maintain steady operation and consistent product quality.[311] Increasing solid content from 5–10 wt% to >20 wt% improves EG concentration and reduces downstream energy use, but introduces mass-transfer limitations due to slurry viscosity. Optimized hydrodynamics have enabled EG yields of 40–65% even at high solids.[67] Continuous solid feeding using screw or piston pumps allows direct hydrogenolysis of wet or dry biomass under pressure,[51] though mechanical stability remains a challenge. Alternatively, two-stage strategies—acidic saccharification followed by hydrogenation—achieve high efficiency and controllability. Hilgert *et al.*[68] converted ball-milled cellulose to soluble oligosaccharides using 10 wt% H_2SO_4, which were subsequently hydrogenolyzed to hexitols with greatly improved activity.

Downstream separation is another decisive cost factor. Because ethanol, EG, 1,2-PG, and 1,2-BDO differ in boiling points by only 3–10 K, conventional distillation is energy-intensive. Alternatives such as pervaporation membranes,

reactive distillation, or selective catalytic upgrading offer promising low-energy options. Polymer-grade EG (>98%) is required for polyethylene terephthalate (PET) synthesis.[320] Minor 1,2-PG or 1,2-BDO impurities (<2 wt%) have a negligible impact on PET properties. Nevertheless, standardized specifications for bio-based alcohols must be established to ensure downstream compatibility and market acceptance.

A landmark demonstration was achieved in October 2024, when the "thousand-ton-scale one-step catalytic conversion of biomass to EG" pilot plant—jointly developed by the Dalian Institute of Chemical Physics (Academician Zhang Tao) and Zhongke Baiyijin New Energy—passed national appraisal.[321] Operating continuously for 72 h, the process reached ≈80% EG selectivity and 99.9% purity, satisfying polymer-grade standards. The Ni–W catalytic system and efficient separation sequence confirmed the feasibility of direct biomass-to-EG conversion under mild, energy-saving conditions. The resulting bio-EG has been successfully applied in manufacturing bio-PET, polyethylene furanoate (PEF), and fine-chemical aromatics, offering a tangible pathway toward industrial decarbonization.

Overall, the integration of advanced catalytic systems with reactor engineering, high-solid processing, and low-energy separations has transformed cellulose hydrogenolysis from a mechanistic model into a practicable industrial technology. Continued progress will rely on cross-scale integration—linking rational catalyst design, operando mechanistic insight, feedstock preprocessing, reactor hydrodynamics, and separation intensification. As global chemical production shifts toward renewable carbon and circular-economy paradigms, such convergence will be decisive for achieving economically viable, carbon-neutral manufacture of bio-based low-carbon alcohols and related platform molecules.

6 Challenges and future opportunities

The catalytic hydrogenolysis of cellulose to low-carbon alcohols has advanced from fundamental mechanistic insight to encouraging pilot-scale demonstrations. Yet, the translation of this progress into robust, scalable technology will require deeper convergence between molecular catalysis, materials design, and process engineering.

Mechanistic studies have established a coherent picture of the reaction network, identifying cellulose depolymerization and glucose retro-aldol condensation as the kinetically demanding steps. Although substantial progress has been made in correlating tungsten redox chemistry, proton transfer, and hydride delivery, the intrinsic activation barriers of these transformations remain high. A key challenge is thus the development of catalytic environments capable of dynamically stabilizing transient intermediates and lowering reaction energies through coupled proton–hydride pathways. Continued integration of operando spectroscopy, transient kinetic analysis, and microkinetic modelling will be central to revealing active motifs and informing mechanism-driven design.

From a materials perspective, bifunctional systems, particularly tungsten-based acid–metal ensembles and spatially confined nanostructures, have provided a conceptual platform for unifying hydrolysis, isomerization, C–C scission, and hydrogenation. However, hydrothermal stability, structural complexity, and susceptibility to leaching continue to limit long-term performance. Opportunities lie in strategies that impart atomic-level precision—single-atom dispersion, defect engineering, and self-regulating oxide-metal interfaces capable of maintaining activity under dynamic reaction conditions. Hierarchically organized microenvironments that choreograph reaction sequences within confined domains offer another route to simultaneously enhance selectivity and durability.

Notably, single-atom catalysts (SACs) provide a highly promising pathway for achieving catalytic design with atomic-level precision by maximizing the utilization efficiency of metal atoms and constructing unique active microenvironments. For instance, the elaborately designed Ru single-atom catalyst combined with sulfonic acid and nitrogen sites (Ru–SO_3H–N) has achieved a significantly enhanced yield in the hydrogenolysis of cellulose to 1,2-PG.[322] This is attributed to the optimized electronic structure of Ru sites, which can simultaneously improve key steps such as cellulose hydrolysis and fructose hydrogenolysis. Similarly, integrating high-density ruthenium single atoms (10.1 wt%) into sulfonic acid-functionalized hollow mesoporous carbon enables efficient catalysis of the cascade reaction of cellulose conversion to isosorbide *via* sorbitol,[323] where Ru single-atom sites play a crucial role in the selective hydrogenation of glucose intermediates. Beyond noble metals, durable nickel single-atom catalysts (Ni–N–C) have also demonstrated potential in efficiently catalyzing cellulose conversion reactions under harsh conditions, offering a possibility for reducing catalyst costs.[324] These advances highlight the unique advantage of SACs in synergistically catalyzing multiple sequential reactions in cellulose conversion through the precise regulation of the coordination environment of metal centers.

Selectivity control—central to producing EG, 1,2-PG, ethanol, or polyols—illustrates the importance of kinetic steering rather than thermodynamic preference. The next phase of catalyst design will require embedding selectivity determinants into the architecture itself through electronic tuning and spatial programming, reducing reliance on external operational constraints. Machine-learning-assisted discovery of structure-selectivity descriptors is expected to accelerate this transition toward programmable catalytic systems.

Process engineering considerations remain equally decisive. While semi-continuous and continuous-flow reactors have established links between intrinsic kinetics and scalable operation, challenges associated with high-solids processing, mass-transfer limitations, and catalyst fouling persist. Progress will depend on process-intensified reactor concepts that integrate hydrogenolysis, separation, and catalyst regeneration, as well as on catalysts tolerant to feedstock heterogeneity. The co-development of low-energy pretreatment strategies and robust catalytic systems is critical for ensuring broad feedstock compatibility and reducing operational complexity.

Looking forward, several research directions appear particularly promising: (1) unconventional product pathways: exploring novel transformation paradigms, such as the directed synthesis of methanol from cellulose, which requires innovative catalyst design and reaction engineering to control deep C–C bond cleavage. (2) Dynamic multifunctional catalysis: developing catalysts capable of *in situ* restructuring or valence switching (*e.g.*, W^{6+}/W^{5+}, Sn^{4+}/Sn^{2+}) to adaptively couple hydrolysis, isomerization, and hydrogenation under reaction conditions. (3) Advanced confinement materials: employing novel confinement materials with designable pores and tunable acid–base properties (such as metal organic frameworks, covalent organic frameworks, and modified layered clays) to create precise microenvironments for cascade reactions in cellulose hydrogenolysis. (4) Atomic and interfacial precision: utilizing single-atom anchoring, dual-site ensembles, and well-defined oxide-metal interfaces to regulate elementary reaction steps and suppress over-hydrogenation. (5) Data-driven catalyst discovery: integrating high-throughput experimentation with machine learning and DFT calculations to identify structure–activity descriptors governing selectivity toward C_2–C_3 alcohols. (6) Integrated reaction-separation modules: combining catalytic hydrogenolysis with membrane separation, reactive distillation, or electrochemical hydrogen management to improve carbon efficiency and reduce energy input. (7) Whole-biomass valorization: extending cellulose-focused studies toward integrated lignocellulosic biorefineries that simultaneously valorize cellulose, hemicellulose, and lignin.

The recent demonstration of thousand-ton-scale biomass-to-EG production underscores the growing maturity of this field and its movement toward industrial relevance. As catalytic innovation increasingly aligns with process design and digital optimization, cellulose hydrogenolysis is poised to contribute meaningfully to a low-carbon chemical economy. Ultimately, the one-step catalytic transformation of renewable carbohydrates into platform alcohols exemplifies a broader paradigm: the integration of molecular precision with systems-level engineering to enable sustainable, carbon-neutral chemical manufacturing.

Author contributions

Y. Cui: data curation, formal analysis, investigation, validation, visualization, writing-original draft. D. Wang: investigation, validation, visualization. H. Ben: project administration, resources. X. Su: investigation, validation, supervision, writing-review & editing. X. Yang: conceptualization, formal analysis, investigation, funding acquisition, project administration, resources, writing-review & editing. Y. Huang: project administration, resources.

Conflicts of interest

The authors declare that they have no known competing financial interests or personal relationships that could have appeared to influence the work reported in this paper.

Data availability

No primary research results, software or code have been included and no new data were generated or analysed as part of this review.

Acknowledgements

This work was financially supported by the National Natural Science Foundation of China (Grant No. 22478209, 22478383), the Natural Science Foundation of Shandong Province (Grant No. ZR2024YQ018), the Youth Innovation Team Project of the Shandong Provincial Department of Education (Grant No. 2023KJ356), the Youth Science and Technology Talent Lifting Project of Shandong Province (Grant No. SDAST2024QTA042).

References

1 S. Zangoei, N. Salehnia and M. K. Mashhadi, *Environ. Sci. Pollut. Res.*, 2021, **28**, 19799–19809.
2 A. M. Ruppert, K. Weinberg and R. Palkovits, *Angew. Chem., Int. Ed.*, 2012, **51**, 2564–2601.
3 J. C. Serrano-Ruiz, R. Luque and A. Sepulveda-Escribano, *Chem. Soc. Rev.*, 2011, **40**, 5266–5281.
4 P. Yang, H. Kobayashi and A. Fukuoka, *Chin. J. Catal.*, 2011, **32**, 716–722.
5 S. Wang, A. Cheng, F. Liu, J. Zhang, T. Xia, X. Zeng, W. Fan and Y. Zhang, *Ind. Chem. Mater.*, 2023, **1**, 188–206.
6 Biomass Market Size, Share and Growth Trend Report, 2026–2035, https://www.researchnester.com/cn/reports/biomass-market/1355.
7 X. Zhang, K. Wilson and A. F. Lee, *Chem. Rev.*, 2016, **116**, 12328–12368.
8 Y. C. Feng, S. S. Long, X. Tang, Y. Sun, R. Luque, X. H. Zeng and L. Lin, *Chem. Soc. Rev.*, 2021, **50**, 6042–6093.
9 B. M. Upton and A. M. Kasko, *Chem. Rev.*, 2016, **116**, 2275–2306.
10 H. C. Ong, K. L. Yu, W.-H. Chen, M. K. Pillejera, X. Bi, K.-Q. Tran, A. Pétrissans and M. Pétrissans, *Renew. Sustain. Energy Rev.*, 2021, **152**, 111698.
11 D. M. Alonso, J. Q. Bond and J. A. Dumesic, *Green Chem.*, 2010, **12**, 1493–1513.
12 M. Kumar, A. O. Oyedun and A. Kumar, *Renew. Sustain. Energy Rev.*, 2018, **81**, 1742–1770.
13 H. Li, A. Bunrit, N. Li and F. Wang, *Chem. Soc. Rev.*, 2020, **49**, 3748–3763.
14 W. Gong, Y. Lin, C. Chen, M. Al-Mamun, H. S. Lu, G. Wang, H. Zhang and H. Zhao, *Adv. Mater.*, 2019, **31**, e1808341.
15 C. Li, X. Zhao, A. Wang, G. W. Huber and T. Zhang, *Chem. Rev.*, 2015, **115**, 11559–11624.
16 IRENA, *Global Energy Transformation: A Roadmap to 2050*, International Renewable Energy Agency, 2018, http://refhub.elsevier.com/S2589-5974(19)30149-2/rf0005.
17 M. E. Himmel, S. Ding, D. K. Johnson, W. S. Adney, M. R. Nimlos, J. W. Brady and T. D. Foust, *Science*, 2007, **315**, 804–807.

18 R. M. Wahlström and A. Suurnäkki, *Green Chem.*, 2015, **17**, 694–714.
19 G. W. Huber, S. Iborra and A. Corma, *Chem. Rev.*, 2006, **106**, 4044–4098.
20 N. Wei, J. Quarterman, S. R. Kim, J. H. D. Cate and Y.-S. Jin, *Nat. Commun.*, 2013, **4**, 2580.
21 Y. Sun and J. Cheng, *Bioresour. Technol.*, 2002, **83**, 1–11.
22 M. Li, W. Zhao, Y. Xu, Y. Zhao, K. Yang, W. Tao and J. Xiao, *Ind. Eng. Chem. Res.*, 2019, **58**, 19179–19188.
23 Y. Weng, X. Wang and Y. Zhang, *Trends Chem.*, 2022, **4**, 374–377.
24 C. Luo, S. Wang and H. Liu, *Angew. Chem., Int. Ed.*, 2007, **46**, 7636–7639.
25 A. Fukuoka and P. L. Dhepe, *Angew. Chem., Int. Ed.*, 2006, **45**, 5161–5163.
26 M. Yang, H. Qi, F. Liu, Y. Ren, X. Pan, L. Zhang, X. Liu, H. Wang, J. Pang, M. Zheng, A. Wang and T. Zhang, *Joule*, 2019, **3**, 1937–1948.
27 D. Chu, Z. Luo, Y. Xin, C. Jiang, S. Gao, Z. Wang and C. Zhao, *Fuel*, 2021, **292**, 120311.
28 H. Song, P. Wang, S. Li, W. Deng, Y. Li, Q. Zhang and Y. Wang, *Chem. Commun.*, 2019, **55**, 4303–4306.
29 Q. Liu, H. Wang, H. Xin, C. Wang, L. Yan, Y. Wang, Q. Zhang, X. Zhang, Y. Xu, G. W. Huber and L. Ma, *ChemSusChem*, 2019, **12**, 3977–3987.
30 Y. Wu, C. Dong, H. Wang, J. Peng, Y. Li, C. Samart and M. Ding, *ACS Sustainable Chem. Eng.*, 2022, **10**, 2802–2810.
31 J. Zhang, B. Hou, A. Wang, Z. Li, H. Wang and T. Zhang, *AIChE J.*, 2015, **61**, 224–238.
32 J. Zhang, B. Hou, A. Wang, Z. Li, H. Wang and T. Zhang, *AIChE J.*, 2014, **60**, 3804–3813.
33 G. Zhao, M. Zheng, J. Zhang, A. Wang and T. Zhang, *Ind. Eng. Chem. Res.*, 2013, **52**, 9566–9572.
34 J. Pang, M. Zheng, A. Wang and T. Zhang, *Ind. Eng. Chem. Res.*, 2011, **50**, 6601–6608.
35 L. Zhang, B. Zhan, Y. He, Y. Deng, H. Ji, S. Peng and L. Yan, *Green Chem.*, 2024, **26**, 8794–8807.
36 W. H. Zartman and H. Adkins, *J. Am. Chem. Soc.*, 1933, **55**, 4559–4563.
37 E. I. Du Pont De Nemours & Co, GB1933035971, 1933.
38 M. S. S. R. Tanikella, EP1982303832, 1982.
39 U. Saxena, N. Dwivedi and S. R. Vidyarthi, *Ind. Eng. Chem. Res.*, 2005, **44**, 1466–1473.
40 N. Ji, T. Zhang, M. Zheng, A. Wang, H. Wang, X. Wang and J. G. Chen, *Angew. Chem., Int. Ed.*, 2008, **47**, 8510–8513.
41 M. Zheng, A. Wang, J. Pang, N. Li and T. Zhang, Mechanism and Kinetic Analysis of the Hydrogenolysis of Cellulose to Polyols, in *Reaction Pathways and Mechanisms in Thermocatalytic Biomass Conversion I: Cellulose Structure, Depolymerization and Conversion by Heterogeneous Catalysts*, ed. Schlaf, M., Zhang, Z. C., Springer, Berlin, 2016, pp 227–260.
42 A. Wang and T. Zhang, *Acc. Chem. Res.*, 2013, **46**, 1377–1386.
43 M. Zheng, J. Pang, A. Wang and T. Zhang, *Chin. J. Catal.*, 2014, **35**, 602–613.
44 I. Delidovich, P. J. C. Hausoul, L. Deng, R. Pfützenreuter, M. Rose and R. Palkovits, *Chem. Rev.*, 2016, **116**, 1540–1599.
45 Y. Qiao, G. J. Xia, W. Cao, K. H. Zeng, Q. L. Guo, X. F. Yang, A. Q. Wang and Y. G. Wang, *J. Catal.*, 2023, **427**, 115114.
46 H. S. Kambo and A. Dutta, *Renew. Sustain. Energy Rev.*, 2015, **45**, 359–378.
47 X. Wang, T. You, W. Zheng, X. Li, S. Chen and F. Xu, *Chem. Eng. J.*, 2024, **483**, 148841.
48 N. Yan and S. Ding, *Trends Chem.*, 2019, **1**, 457–458.
49 D. Chu, Y. Xin and C. Zhao, *Chin. J. Catal.*, 2021, **42**, 844–854.
50 K. Tomishige, M. Yabushita, J. Cao and Y. Nakagawa, *Green Chem.*, 2022, **24**, 5652–5690.
51 M. Zheng, J. Pang, R. Sun, A. Wang and T. Zhang, *ACS Catal.*, 2017, **7**, 1939–1954.
52 C. Montassier, D. Giraud and J. Barbier, *Stud. Surf. Sci. Catal.*, 1988, **41**, 165–170.
53 K. Wang, M. C. Hawley and T. D. Furney, *Ind. Eng. Chem. Res.*, 1995, **34**, 3766–3770.
54 J. Zhang, F. Lu, W. Yu, J. Chen, S. Chen, J. Gao and J. Xu, *Catal. Today*, 2014, **234**, 107–112.
55 N. Li and G. W. Huber, *J. Catal.*, 2010, **270**, 48–59.
56 G. Liang, L. He, H. Cheng, W. Li, X. Li, C. Zhang, Y. Yu and F. Zhao, *J. Catal.*, 2014, **309**, 468–476.
57 J. Xi, D. Ding, Y. Shao, X. Liu, G. Lu and Y. Wang, *ACS Sustainable Chem. Eng.*, 2014, **2**, 2355–2362.
58 W. Luo, P. C. A. Bruijnincx and B. M. Weckhuysen, *J. Catal.*, 2014, **320**, 33–41.
59 B. Zhang, X. Li, Q. Wu, C. Zhang, Y. Yu, M. Lan, X. Wei, Z. Ying, T. Liu, G. Liang and F. Zhao, *Green Chem.*, 2016, **18**, 3315–3323.
60 J. Sun and H. Liu, *Green Chem.*, 2011, **13**, 135–142.
61 N. Déchamp, A. Gamez, A. Perrard and P. Gallezot, *Catal. Today*, 1995, **24**, 29–34.
62 H. Kishida, F. Jin, X. Yan, T. Moriya and H. Enomoto, *Carbohydr. Res.*, 2006, **341**, 2619–2623.
63 X. Yan, F. Jin, K. Tohji, A. Kishita and H. Enomoto, *AIChE J.*, 2010, **56**, 2727–2733.
64 D. K. Mishra, A. A. Dabbawala, J. J. Park, S. H. Jhung and J. S. Hwang, *Catal. Today*, 2014, **232**, 99–107.
65 T. Komanoya, H. Kobayashi, K. Hara, W.-J. Chun and A. Fukuoka, *ChemCatChem*, 2014, **6**, 230–236.
66 G. Zhao, M. Zheng, R. Sun, Z. Tai, J. Pang, A. Wang, X. Wang and T. Zhang, *AIChE J.*, 2017, **63**, 2072–2080.
67 J. Pang, M. Zheng, A. Wang, R. Sun, H. Wang, Y. Jiang and T. Zhang, *AIChE J.*, 2014, **60**, 2254–2262.
68 J. Hilgert, N. Meine, R. Rinaldi and F. Schüth, *Energy Environ. Sci.*, 2013, **6**, 92–96.
69 J. Pang, A. Wang, M. Zheng, Y. Zhang, Y. Huang, X. Chen and T. Zhang, *Green Chem.*, 2012, **14**, 614–617.
70 E. Crezee, B. W. Hoffer, R. J. Berger, M. Makkee, F. Kapteijn and J. A. Moulijn, *Appl. Catal., A*, 2003, **251**, 1–17.
71 M. Y. Zheng, A. Q. Wang, N. Ji, J. F. Pang, X. D. Wang and T. Zhang, *ChemSusChem*, 2010, **3**, 63–66.
72 M. J. Ahmed, *Heat Mass Transf.*, 2012, **48**, 343–347.
73 L. Shuai and X. Pan, *Energy Environ. Sci.*, 2012, **5**, 6889–6894.

74 S. Suganuma, K. Nakajima, M. Kitano, D. Yamaguchi, H. Kato, S. Hayashi and M. Hara, *J. Am. Chem. Soc.*, 2008, **130**, 12787–12793.
75 Z. Yao, J. Zhao, R. J. Bunting, C. Zhao, P. Hu and J. Wang, *ACS Catal.*, 2021, **11**, 1202–1221.
76 X. Li, Z. Shao, H. Shan and L. Liu, *Green Chem.*, 2025, **27**, 5322–5331.
77 X. Hu, C. Lievens and C.-Z. Li, *ChemSusChem*, 2012, **5**, 1427–1434.
78 G. Chen, C. Fu, W. Zhang, W. Gong, J. Ma, X. Ji, L. Qian, X. Feng, C. Hu, R. Long and Y. Xiong, *Nat. Commun.*, 2025, **16**, 665.
79 J. Zhang, X. Liu, M. Sun, X. Ma and Y. Han, *ACS Catal.*, 2012, **2**, 1698–1702.
80 C. Liu, J. M. Carraher, J. L. Swedberg, C. R. Herndon, C. N. Fleitman and J.-P. Tessonnier, *ACS Catal.*, 2014, **4**, 4295–4298.
81 J. M. Carraher, C. N. Fleitman and J.-P. Tessonnier, *ACS Catal.*, 2015, **5**, 3162–3173.
82 L. Ren, Q. Guo, P. Kumar, M. Orazov, D. Xu, S. M. Alhassan, K. Andre Mkhoyan, M. E. Davis and M. Tsapatsis, *Angew. Chem., Int. Ed.*, 2015, **127**, 10998–11001.
83 T. Deng and H. Liu, *Green Chem.*, 2013, **15**, 116–124.
84 R. Sun, M. Zheng, J. Pang, X. Liu, J. Wang, X. Pan, A. Wang, X. Wang and T. Zhang, *ACS Catal.*, 2016, **6**, 191–201.
85 Z. Xiao, J. Mao, C. Jiang, C. Xing, J. Ji and Y. Cheng, *J. Renew. Sustain. Energy*, 2017, **9**, 024703.
86 Z. Xiao, S. Jin, M. Pang and C. Liang, *Green Chem.*, 2013, **15**, 891–895.
87 Z. Xiao, S. Jin, G. Sha, C. T. Williams and C. Liang, *Ind. Eng. Chem. Res.*, 2014, **53**, 8735–8743.
88 T. Deng, J. Sun and H. Liu, *Sci. China Chem.*, 2010, **53**, 1476–1480.
89 M. Moliner, Y. Roman-Leshkov and M. E. Davis, *Proc. Natl. Acad. Sci. U. S. A.*, 2010, **107**, 6164–6168.
90 R. Bermejo-Deval, R. S. Assary, E. Nikolla, M. Moliner, Y. Roman-Leshkov, S. J. Hwang, A. Palsdottir, D. Silverman, R. F. Lobo, L. A. Curtiss and M. E. Davis, *Proc. Natl. Acad. Sci. U. S. A.*, 2012, **109**, 9727–9732.
91 Y. Cao, J. Wang, M. Kang and Y. Zhu, *RSC Adv.*, 2015, **5**, 90904–90912.
92 X. Yang, Z. Li, M. Guo, T. Zhao, X. Su, W. Jiang, G. Han and H. Ben, *Fuel*, 2023, **341**, 127560.
93 C. Liu, C. Zhang, S. Sun, K. Liu, S. Hao, J. Xu, Y. Zhu and Y. Li, *ACS Catal.*, 2015, **5**, 4612–4623.
94 Y. Liu, C. Luo and H. Liu, *Angew. Chem., Int. Ed.*, 2012, **51**, 3249–3253.
95 C. Li, G. Xu, C. Wang, L. Ma, Y. Qiao, Y. Zhang and Y. Fu, *Green Chem.*, 2019, **21**, 2234–2239.
96 N. Li, Y. Zheng, L. Wei, H. Teng and J. Zhou, *Green Chem.*, 2017, **19**, 682–691.
97 J. J. Wiesfeld, P. Peršolja, F. A. Rollier, A. M. Elemans-Mehring and E. J. M. Hensen, *Mol. Catal.*, 2019, **473**, 110400.
98 K. Fabičovicová, M. Lucas and P. Claus, *Green Chem.*, 2015, **17**, 3075–3083.
99 L. S. Ribeiro, J. Órfão, J. J. de Melo Órfão and M. F. R. Pereira, *Cellulose*, 2018, **25**, 2259–2272.
100 L. S. Ribeiro, J. J. Melo Órfão and M. F. R. Pereira, *Bioresour. Technol.*, 2018, **263**, 402–409.
101 L. S. Ribeiro, N. Rey-Raap, J. L. Figueiredo, J. J. Melo Órfão and M. F. R. Pereira, *Cellulose*, 2019, **26**, 7337–7353.
102 Z. Yang, R. Huang, W. Qi, L. Tong, R. Su and Z. He, *Chem. Eng. J.*, 2015, **280**, 90–98.
103 K. Zhang, G. Yang, G. Lyu, Z. Jia, L. A. Lucia and J. Chen, *ACS Sustainable Chem. Eng.*, 2019, **7**, 11110–11117.
104 J. W. Han and H. Lee, *Catal. Commun.*, 2012, **19**, 115–118.
105 M. Qiu, J. Zheng, Y. Yao, L. Liu, X. Zhou, H. Jiao, J. Aarons, K. Zhang, Q. Guan and W. Li, *J. Clean. Prod.*, 2022, **362**, 132364.
106 P. A. Lazaridis, S. A. Karakoulia, C. Teodorescu, N. Apostol, D. Macovei, A. Panteli, A. Delimitis, S. M. Comand, V. I. Parvulescud and K. S. Triantafyllidis, *Appl. Catal., B*, 2017, **214**, 1–14.
107 M. C. M. Castoldi, L. D. T. Câmara, R. S. Monteiro, A. M. Constantino, L. Camacho, J. W. de M. Carneiro and D. A. G. Aranda, *React. Kinet. Catal. Lett.*, 2007, **91**, 341–352.
108 H. Kobayashi, Y. Ito, T. Komanoya, Y. Hosaka, P. L. Dhepe, K. Kasai, K. Haraa and A. Fukuoka, *Green Chem.*, 2011, **13**, 326–333.
109 J. Xi, Y. Zhang, Q. Xia, X. Liu, J. Ren, G. Lu and Y. Wang, *Appl. Catal., A*, 2013, **459**, 52–58.
110 A. Negoi, K. Triantafyllidis, V. I. Parvulescu and S. M. Coman, *Catal. Today*, 2014, **223**, 122–128.
111 A. Romero, D. A. Cantero, A. Nieto-Márquez, C. Martínez, E. Alonso and M. J. Cocero, *Green Chem.*, 2016, **18**, 4051–4062.
112 O. V. Manaenkov, V. G. Matveeva, E. M. Sulman, A. E. Filatova, O. Y. Makeeva, O. V. Kislitza, A. I. Sidorov, V. Y. Doluda and M. G. Sulman, *Top. Catal.*, 2014, **57**, 1476–1482.
113 N. V. Gromov, T. B. Medvedeva, O. P. Taran, M. N. Timofeeva, O. Said-Aizpuru, V. N. Panchenko, E. Y. Gerasimov, I. V. Kozhevnikov and V. N. Parmon, *Appl. Catal., A*, 2020, **595**, 117489.
114 Z. Tai, J. Zhang, A. Wang, M. Zheng and T. Zhang, *Chem. Commun.*, 2012, **48**, 7052–7054.
115 J. Chai, S. Zhu, Y. Cen, J. Guo, J. Wang and W. Fan, *RSC Adv.*, 2017, **7**, 8567–8574.
116 R. Palkovits, K. Tajvidi, J. Procelewska, R. Rinaldi and A. Ruppert, *Green Chem.*, 2010, **12**, 972–978.
117 K. Shimizu, H. Furukawa, N. Kobayashi, Y. Itaya and A. Satsuma, *Green Chem.*, 2009, **11**, 1627–1632.
118 E. N. Dorokhova and I. P. Alimarin, *Russ. Chem. Rev.*, 1979, **48**, 502–516.
119 S. Yu, X. Cao, S. Liu, L. Li and Q. Wu, *RSC Adv.*, 2018, **8**, 24857–24865.
120 A. R. Mankar, A. Modak and K. K. Pant, *Fuel Process. Technol.*, 2021, **218**, 106847.
121 R. Palkovits, K. Tajvidi, A. M. Ruppert and J. Procelewska, *Chem. Commun.*, 2011, **47**, 576–578.
122 G. Liang, C. Wu, L. He, J. Ming, H. Cheng, L. Zhuo and F. Zhao, *Green Chem.*, 2011, **13**, 839–842.

123 W. Deng, X. Tan, W. Fang, Q. Zhang and Y. Wang, *Catal. Lett.*, 2009, **133**, 167–174.
124 J. Geboers, S. Van de Vyver, K. Carpentier, P. Jacobs and B. Sels, *Chem. Commun.*, 2011, **47**, 5590–5592.
125 J. Geboers, S. Van de Vyver, K. Carpentier, K. de Blochouse, P. Jacobs and B. Sels, *Chem. Commun.*, 2010, **46**, 3577–3579.
126 B. Op de Beeck, J. Geboers, S. Van de Vyver, J. V. Lishout, J. Snelders, W. J. J. Huijgen, C. M. Courtin, P. A. Jacobs and B. F. Sels, *ChemSusChem*, 2013, **6**, 199–208.
127 Y. Yang, D. Ren, C. L. Shang, Z. Ding and X. Luo, *Chem. Eng. J.*, 2023, **452**, 139206.
128 S. Suganuma, K. Nakajima, M. Kitano, D. Yamaguchi, H. Kato, S. Hayashi and M. Hara, *J. Am. Chem. Soc.*, 2008, **130**, 12787–12793.
129 J. Pang, A. Wang, M. Zheng and T. Zhang, *Chem. Commun.*, 2010, **46**, 6935–6937.
130 T. Komanoya, H. Kobayashi, K. Hara, W. J. Chun and A. Fukuoka, *Appl. Catal., A*, 2011, **407**, 188–194.
131 K. Fabičovicová, O. Malter, M. Lucas and P. Claus, *Green Chem.*, 2014, **16**, 3580–3588.
132 K. Nakajima, Y. Baba, R. Noma, M. Kitano, J. N. Kondo, S. Hayashi and M. Hara, *J. Am. Chem. Soc.*, 2011, **133**, 4224–4227.
133 N. Li, Z. Ji, L. Wei, Y. Zheng, Q. Shen, Q. Ma, M. Tan, M. Zhan and J. Zhou, *Bioresour. Technol.*, 2018, **264**, 58–65.
134 L. S. Ribeiro, J. J. Delgado, J. J. de Melo Órfão and M. F. R. Pereira, *Catal. Today*, 2017, **279**, 244–251.
135 L. S. Ribeiro, J. J. M. Órfão and M. F. R. Pereira, *Green Chem.*, 2015, **17**, 2973–2980.
136 L. S. Ribeiro, J. J. Delgado, J. J. M. Órfão and M. F. R. Pereira, *Appl. Catal., B*, 2017, **217**, 265–274.
137 X. Xiao, S. H. Lim, W. Chu and Y. Liu, *ACS Sustainable Chem. Eng.*, 2021, **9**, 12655–12662.
138 S. Carlier, J. Gripekoven, M. Philippo and S. Hermans, *Appl. Catal., B*, 2021, **282**, 119515.
139 J. Yang, L. Liu, H. Zhang, M. Qiu, Q. Guan and W. Li, *ACS Sustainable Chem. Eng.*, 2023, **11**, 15663–15673.
140 D. Lai, L. Deng, Q. Guo and Y. Fu, *Energy Environ. Sci.*, 2011, **4**, 3552–3557.
141 C. Zhang, H. Wang, F. Liu, L. Wang and H. He, *Cellulose*, 2013, **20**, 127–134.
142 I. Podolean, A. Negoi, N. Candu, M. Tudorache, V. I. Parvulescu and S. M. Coman, *Top. Catal.*, 2014, **57**, 1463–1469.
143 O. V. Manaenkov, J. J. Mann, O. V. Kislitza, Y. Losovyj, B. D. Stein, D. G. Morgan, M. Pink, O. L. Lependina, Z. B. Shifrina, V. G. Matveeva, E. M. Sulman and L. M. Bronstein, *ACS Appl. Mater. Interfaces*, 2016, **8**, 21285–21293.
144 M. Lv, Q. Xin, D. Yin, Z. Jia, C. Yu, T. Wang, S. Yu, S. Liu, L. Li and Y. Liu, *ACS Sustainable Chem. Eng.*, 2020, **8**, 3617–3625.
145 Y. Liu and H. Liu, *Catal. Today*, 2016, **269**, 74–81.
146 L. S. Ribeiro, J. J. de Melo Órfão and M. F. R. Pereira, *Bioresour. Technol.*, 2017, **244**, 1173–1177.
147 N. Rey-Raap, L. S. Ribeiro, J. J. de Melo Órfão, J. L. Figueiredo and M. F. R. Pereira, *Appl. Catal., B*, 2019, **256**, 117826.
148 L. S. Ribeiro, J. J. de Melo Órfão and M. F. R. Pereira, *Bioresour. Technol.*, 2017, **232**, 152–158.
149 S. Esposito, B. Silvestri, V. Russo, B. Bonelli, M. Manzoli, F. A. Deorsola, A. Vergara, A. Aronne and M. D. Serio, *ACS Catal.*, 2019, **9**, 3426–3436.
150 A. Yepez, A. Pineda, A. Garcia, A. A. Romero and R. Luque, *Phys. Chem. Chem. Phys.*, 2013, **15**, 12165–12172.
151 J. Zhang, B. Hou, X. Wang, Z. Li, A. Wang and T. Zhang, *J. Energy Chem.*, 2015, **24**, 9–14.
152 Y. Liu, Y. Liu, Q. Wu and Y. Zhang, *Catal. Commun.*, 2019, **129**, 105731.
153 Y. Liu, Y. Liu and Y. Zhang, *Appl. Catal., B*, 2019, **242**, 100–108.
154 J. Ji, Y. Xu, Y. Liu and Y. Zhang, *Catal. Commun.*, 2020, **144**, 106074.
155 Y. Hirano, K. Sagata and Y. Kita, *Appl. Catal., A*, 2015, **502**, 1–7.
156 J. Pang, M. Zheng, X. Li, Y. Jiang, Y. Zhao, A. Wang, J. Wang, X. Wang and T. Zhang, *Appl. Catal., B*, 2018, **239**, 300–308.
157 M. Besson, P. Gallezot, A. Perrard and C. Pinel, *Catal. Today*, 2005, **102–103**, 160–165.
158 T. Kilpiö, A. Aho, D. Murzin and T. Salmi, *Ind. Eng. Chem. Res.*, 2013, **52**, 7690–7703.
159 V. N. Sapunov, M. Y. Grigoryev, E. M. Sulman and M. B. Konyaeva, *J. Phys. Chem. A*, 2013, **117**, 4073–4083.
160 A. Aho, S. Roggan, O. A. Simakova, T. Salmi and D. Y. Murzin, *Catal. Today*, 2015, **241**, 195–199.
161 B. W. Hoffer, E. Crezee, P. R. M. Mooijman, A. D. van Langeveld, F. Kapteijn and J. A. Moulijn, *Catal. Today*, 2003, **79**, 35–41.
162 V. Russo, T. Kilpio, M. Di Serio, R. Tesser, E. Santacesaria, D. Y. Murzin and T. Salmi, *Chem. Eng. Res. Des.*, 2015, **102**, 171–185.
163 M. Besson and P. Gallezot, *Catal. Today*, 2003, **81**, 547–559.
164 B. J. Arena, *Appl. Catal., A*, 1992, **87**, 219–229.
165 D. K. Mishra, J. M. Lee, J. S. Chang and J. S. Hwang, *Catal. Today*, 2012, **185**, 104–108.
166 M. Yadav, D. K. Mishra and J. S. Hwang, *Appl. Catal., A*, 2012, **425**, 110–116.
167 J. Zhang, L. Lin, J. Zhang and J. Shi, *Carbohydr. Res.*, 2011, **346**, 1327–1332.
168 A. Romero, A. Nieto-Maŕquez and E. Alonso, *Appl. Catal., A*, 2017, **529**, 49–59.
169 D. K. Mishra, A. A. Dabbawala and J. S. Hwang, *J. Mol. Catal. A: Chem.*, 2013, **376**, 63–70.
170 X. Yang, X. Li, J. Zhao, J. Liang and J. Zhu, *Molecules*, 2023, **28**, 4830.
171 H.-L. He, Z. Liu, F. Liu, J. Chen, P. Wang, X. Yi, A. Zheng and L. Wang, *J. Mater. Chem. A*, 2024, **12**, 26214–26223.
172 C. Li, G. Xu, X. Zhang and Y. Fu, *Chin. J. Chem.*, 2020, **38**, 453–457.
173 Y. Jia and H. Liu, *Catal. Sci. Technol.*, 2016, **6**, 7042–7052.
174 P. J. C. Hausoul, A. K. Beine, L. Neghadar and R. Palkovits, *Catal. Sci. Technol.*, 2017, **7**, 56–63.

175 D. K. Sohounloue, C. Montassier and J. Barbier, *React. Kinet. Catal. Lett.*, 1983, **22**, 391–397.
176 C. Montassier, J. C. Ménézo, L. C. Hoang, C. Renaud and J. Barbier, *J. Mol. Catal.*, 1991, **70**, 99–110.
177 L. Zhao, J. Zhou, Z. Sui and X. Zhou, *Chem. Eng. Sci.*, 2010, **65**, 30–35.
178 J. Zhou, M. Zhang, L. Zhao, P. Li, X. Zhou and W. Yuan, *Catal. Today*, 2009, **147**, S225–S229.
179 L. Zhao, J. Zhou, G. Yang, Y. Ji, M. Zhang, H. Chen and X. Zhou, *Energy Sources, Part A*, 2012, **34**, 430–438.
180 X. Guo, J. Guan, B. Li, X. Wang, X. Mu and H. Liu, *Sci. Rep.*, 2015, **5**, 16451.
181 X. Guo, H. Dong, B. Li, L. Dong, X. Mu and X. Chen, *J. Mol. Catal. A: Chem.*, 2017, **426**, 79–87.
182 I. M. Leo, M. L. Granados, J. L. G. Fierro and R. Mariscal, *Chin. J. Catal.*, 2014, **35**, 614–621.
183 B. Gumina, C. Espro, S. Galvagno, R. Pietropaolo and F. Mauriello, *ACS Omega*, 2019, **4**, 352–357.
184 G. F. Leal, S. F. Moya, D. M. Meira, D. H. Barrett, E. Teixeira-Neto, A. A. S. Curvelo, V. Teixeira da Silva and C. B. Rodella, *RSC Adv.*, 2016, **6**, 87756–87766.
185 W. Jia, H. Song, D. Wang, C. Zhou, Y. Zhao, Y. Cui, H. Ben and X. Yang, *ACS Sustainable Chem. Eng.*, 2025, **13**, 13274–13283.
186 W. Jia, W. Liu, Y. Cui, H. Song, C. Zhou, W. Jiang, H. Ben, X. Yang and D. Chen, *J. Catal.*, 2025, **442**, 115860.
187 S. Xu, X. Yan, Q. Bu and H. Xia, *Cellulose*, 2017, **24**, 2403–2413.
188 Q. Xin, L. Jiang, S. Yu, S. Liu, D. Yin, L. Li, C. Xie, Q. Wu, H. Yu, Y. Liu and Y. Liu, *J. Phys. Chem. C*, 2021, **125**, 18170–18179.
189 Y. Cui, D. Wang, C. Zhou, X. Zhang, H. Ben and X. Yang, *Appl. Catal., B*, 2026, **381**, 125818.
190 Y. Cui, N. Wang, G. Bi, H. Zhuo, X. Shang, T. Cai, W. Jiang, H. Ben, X. Yang and Y. Huang, *Adv. Funct. Mater.*, 2025, **35**, 2421143.
191 Q. Xin, S. Yu, L. Jiang, D. Yin, L. Li, C. Xie, Q. Wu, H. Yu, Y. Liu, Y. Liu and S. Liu, *J. Phys. Chem. C*, 2021, **125**, 6632–6642.
192 M. Lv, Y. Zhang, Q. Xin, D. Yin, S. Yu, S. Liu, L. Li, C. Xie, Q. Wu, H. Yu and Y. Liu, *Chem. Eng. J.*, 2020, **396**, 125274.
193 D. Ekeberg, S. Morgenlie and Y. Stenstrøm, *Carbohydr. Res.*, 2005, **340**, 373–377.
194 Y. Roman-Leshkov and M. E. Davis, *ACS Catal.*, 2011, **1**, 1566–1580.
195 X. Chen, G. Clet, K. Thomas and M. Houalla, *J. Catal.*, 2010, **273**, 236–244.
196 T. Kim, A. Burrows, C. J. Kiely and I. E. Wachs, *J. Catal.*, 2007, **246**, 370–381.
197 J. Wang, G. Yao, Y. Wang, H. Zhang, Z. Huo and F. Jin, *RSC Adv.*, 2015, **5**, 51435–51439.
198 Y. Jia, Q. Sun and H. Liu, *Appl. Catal., A*, 2020, **603**, 117770.
199 Y. Jia and H. Liu, *Chin. J. Catal.*, 2015, **36**, 1552–1559.
200 L. Yang, X. Yan, Q. Wang, Q. Wang and H. Xia, *Carbohydr. Res.*, 2015, **404**, 87–92.
201 D. Wang, W. Niu, M. Tan, M. Wu, X. Zheng, Y. Li and N. Tsubaki, *ChemSusChem*, 2014, **7**, 1398–1406.
202 E. Girard, D. Delcroix and A. Cabiac, *Catal. Sci. Technol.*, 2016, **6**, 5534–5542.
203 M. Gu, Z. Shen, W. Zhang, M. Xia, J. Jiang, W. Dong, X. Zhou and Y. Zhang, *ChemCatChem*, 2020, **12**, 3447–3452.
204 L. Vilcocq, A. Cabiac, C. Especel, S. Lacombe and D. Duprez, *Catal. Commun.*, 2011, **15**, 18–22.
205 L. Vilcocq, A. Cabiac, C. Especel, S. Lacombe and D. Duprez, *Catal. Today*, 2012, **189**, 117–122.
206 L. Vilcocq, A. Cabiac, C. Especel, S. Lacombe and D. Duprez, *Catal. Today*, 2015, **242**, 91–100.
207 L. Vilcocq, R. Koerin, A. Cabiac, C. Especel, S. Lacombe and D. Duprez, *Appl. Catal., B*, 2014, **148–149**, 499–508.
208 H. Kobayashi, Y. Hosaka, K. Hara, B. Feng, Y. Hirosaki and A. Fukuoka, *Green Chem.*, 2014, **16**, 637–644.
209 S. Van de Vyver, J. Geboers, M. Dusselier, H. Schepers, T. Vosch, L. Zhang, G. Van Tendeloo, P. A. Jacobs and B. F. Sels, *ChemSusChem*, 2010, **3**, 698–701.
210 S. Van de Vyver, J. Geboers, W. Schutyser, M. Dusselier, P. Eloy, E. Dornez, J. W. Seo, C. M. Courtin, E. M. Gaigneaux, P. A. Jacobs and B. F. Sels, *ChemSusChem*, 2012, **5**, 1549–1558.
211 R. Sun, T. Wang, M. Zheng, W. Deng, J. Pang, A. Wang, X. Wang and T. Zhang, *ACS Catal.*, 2015, **5**, 874–883.
212 X. Wang, L. Meng, F. Wu, Y. Jiang, L. Wang and X. Mu, *Green Chem.*, 2012, **14**, 758–765.
213 L. N. Ding, A. Q. Wang, M. Y. Zheng and T. Zhang, *ChemSusChem*, 2010, **3**, 818–821.
214 Y. K. Lee and S. T. Oyama, *J. Catal.*, 2006, **239**, 376–389.
215 P. Yang, H. Kobayashi, K. Hara and A. Fukuoka, *ChemSusChem*, 2012, **5**, 920–926.
216 C. Li, G. Xu, K. Li, C. Wang, Y. Zhang and Y. Fu, *Chem. Commun.*, 2019, **55**, 7663–7666.
217 J. Zhang, S. Wu and Y. Liu, *Energy Fuels*, 2014, **28**, 4242–4246.
218 G. Liang, H. Cheng, W. Li, L. He, Y. Yu and F. Zhao, *Green Chem.*, 2012, **14**, 2146–2149.
219 G. Liang, L. He, M. Arai and F. Zhao, *ChemSusChem*, 2014, **7**, 1415–1421.
220 A. A. Kirali, S. Sreekantan and B. Marimuthu, *New J. Chem.*, 2020, **44**, 15958–15965.
221 Z. Tan, L. Shi, Y. Zan, G. Miao, S. Li, L. Kong, S. Li and Y. Sun, *Appl. Catal., A*, 2018, **560**, 28–36.
222 C. Liu, Y. Shang, S. Wang, X. Liu, X. Wang, J. Gui, C. Zhang, Y. Zhu and Y. Li, *Mol. Catal.*, 2020, **485**, 110514.
223 P. Yazdani, B. Wang, Y. Du, S. Kawi and A. Borgna, *Catal. Sci. Technol.*, 2017, **7**, 4680–4690.
224 L. Ye, X. Duan, H. Lin and Y. Yuan, *Catal. Today*, 2012, **183**, 65–71.
225 Z. Zhou, J. Zhang, J. Qin, D. Li and W. Wu, *J. Phys. Chem. A*, 2018, **92**, 456–465.
226 M. Banu, S. Sivasanker, T. M. Sankaranarayanan and P. Venuvanalingam, *Catal. Commun.*, 2011, **12**, 673–677.
227 M. Banu, P. Venuvanalingam, R. Shanmugam, B. Viswanathan and S. Sivasanker, *Top. Catal.*, 2012, **55**, 897–907.

228 R. Vijaya Shanthi, T. M. Sankaranarayanan, R. Mahalakshmy and S. Sivasanker, *J. Environ. Chem. Eng.*, 2015, **3**, 1752–1757.
229 T. Soták, T. Schmidt and M. Hronec, *Appl. Catal., A*, 2013, **459**, 26–33.
230 X. Jin, J. Shen, W. Yan, M. Zhao, P. S. Thapa, B. Subramaniam and R. V. Chaudhari, *ACS Catal.*, 2015, **5**, 6545–6558.
231 R. Vijaya Shanthi, R. Mahalakshmy, K. Thirunavukkarasu and S. Sivasanker, *Mol. Catal.*, 2018, **451**, 170–177.
232 X. Chen, X. Wang, S. Yao and X. Mu, *Catal. Commun.*, 2013, **39**, 86–89.
233 X. Wang, X. Liu, Y. Xu, G. Peng, Q. Cao and X. Mu, *Chin. J. Catal.*, 2015, **36**, 1614–1622.
234 W. Du, L. Zheng, J. Shi, S. Xia and Z. Hou, *Fuel Process. Technol.*, 2015, **139**, 86–90.
235 W. Du, L. Zheng, X. Li, J. Fu, X. Lu and Z. Hou, *Appl. Clay Sci.*, 2016, **123**, 166–172.
236 X. Cao, Q. Zhang, D. Jiang, Q. Liu, L. Ma, T. Wang and D. Li, *Chin. J. Chem. Phys.*, 2015, **28**, 338–344.
237 C. Cai, H. Wang, H. Xin, C. Zhu, Q. Zhang, X. Zhang, C. Wang, Q. Liu and L. Ma, *RSC Adv.*, 2020, **10**, 3993–4001.
238 Y. Qiao, G. J. Xia, W. Cao, K. H. Zeng, Q. L. Guo, X. F. Yang, A. Q. Wang and Y. G. Wang, *J. Catal.*, 2023, **427**, 115114.
239 Y. Liu, W. Zhang and H. Liu, *Chin. J. Catal.*, 2023, **46**, 56–63.
240 Z. Li, J. Zhang, B. Hou and A. Wang, *AIChE J.*, 2019, **65**, e16585.
241 Y. Liu, W. Zhang, C. Hao, S. Wang and H. Liu, *Proc. Natl. Acad. Sci. U. S. A.*, 2022, **119**, e2206399119.
242 N. Ji, M. Zheng, A. Wang, T. Zhang and J. G. Chen, *ChemSusChem*, 2012, **5**, 939–944.
243 L. Zhou, A. Wang, C. Li, M. Zheng and T. Zhang, *ChemSusChem*, 2012, **5**, 932–938.
244 C. Li, M. Zheng, A. Wang and T. Zhang, *Energy Environ. Sci.*, 2012, **5**, 6383–6390.
245 N. Ji, T. Zhang, M. Zheng, A. Wang, H. Wang, X. Wang, Y. Shu, A. L. Stottlemyer and J. G. Chen, *Catal. Today*, 2009, **147**, 77–85.
246 C. B. Rodella, D. H. Barrett, S. F. Moya, S. J. A. Figueroa, M. T. B. Pimenta, A. A. S. Curvelo and V. Teixeira da Silva, *RSC Adv.*, 2015, **5**, 23874–23885.
247 M. Gao, Z. Li, B. Zhao, S. Yu, L. Huang and Q. Wu, *Fuel Process. Technol.*, 2023, **247**, 107816.
248 Y. Zhang, A. Wang and T. Zhang, *Chem. Commun.*, 2010, **46**, 862–864.
249 G. Zhao, M. Zheng, A. Wang and T. Zhang, *Chin. J. Catal.*, 2010, **31**, 928–932.
250 Z. Tai, J. Zhang, A. Wang, J. Pang, M. Zheng and T. Zhang, *ChemSusChem*, 2013, **6**, 652–658.
251 L. Zhou, J. Pang, A. Wang and T. Zhang, *Chin. J. Catal.*, 2013, **34**, 2041–2046.
252 Y. Cao, J. Wang, M. Kang and Y. Zhu, *J. Mol. Catal. A: Chem.*, 2014, **381**, 46–53.
253 Z. Xiao, J. Mao, J. Ji, R. Sha, Y. Fan and C. Xing, *J. Fuel Chem. Technol.*, 2017, **45**, 641–650.
254 I. G. Baek, S. J. You and E. D. Park, *Bioresour. Technol.*, 2012, **114**, 684–690.
255 M. Gu, Z. Shen, L. Yang, W. Dong, L. Kong, W. Zhang, B. Y. Peng and Y. Zhang, *Sci. Rep.*, 2019, **9**, 11938.
256 Z. Xiao, R. Sha, J. Ji and J. Mao, *J. Fuel Chem. Technol.*, 2016, **44**, 1225–1232.
257 Z. Xiao, Y. Xu, Y. Fan, Q. Zhang, J. Mao and J. Ji, *Asia Pac. J. Chem. Eng.*, 2018, **13**, e2153.
258 Z. Xiao, Y. Fan, Y. Cheng, Q. Zhang, Q. Ge, R. Sha, J. Ji and J. Mao, *Fuel*, 2018, **215**, 406–416.
259 Z. Xiao, Q. Zhang, T. Chen, X. Wang, Y. Fan, Q. Ge, R. Zhai, R. Sun, J. Ji and J. Mao, *Fuel*, 2018, **230**, 332–343.
260 M. Li, Y. Ma, X. Ma, Y. Sun and Z. Song, *RSC Adv.*, 2018, **8**, 10907–10913.
261 M. S. Hamdy, M. A. Eissa and S. M. A. S. Keshk, *Green Chem.*, 2017, **19**, 5144–5151.
262 S. Sreekantan, A. A. Kiralia and B. Marimuthu, *New J. Chem.*, 2021, **45**, 19244–19254.
263 H. Liu, L. Qin, X. Wang, C. Du, D. Sun and X. Meng, *Catal. Commun.*, 2016, **77**, 47–51.
264 N. Li, X. Liu, J. Zhou, Q. Ma, M. Liu and W. Chen, *ACS Sustainable Chem. Eng.*, 2020, **8**, 9650–9659.
265 J. Yu, J. Liang, X. Chen, L. Wang, X. Wei, Y. Li and Y. Qin, *ACS Omega*, 2021, **6**, 11650–11659.
266 D. Chu and C. Zhao, *Catal. Today*, 2020, **351**, 125–132.
267 X. Yang, Z. Li, M. Guo, T. Zhao, X. Su, W. Jiang, G. Han and H. Ben, *Fuel*, 2023, **341**, 127560.
268 H. Wang, X. Hu, S. Liu, C. Cai, C. Zhu, H. Xin, Z. Xiu, C. Wang, Q. Liu, Q. Zhang, X. Zhang and L. Ma, *Cellulose*, 2020, **27**, 7591–7605.
269 Z. Xiao, X. Wang, Q. Yang, C. Xing, Q. Gea, X. Gai, J. Mao and J. Ji, *J. Energy Chem.*, 2020, **50**, 25–36.
270 R. Ooms, M. Dusselier, J. A. Geboers, B. Op de Beeck, R. Verhaeven, E. Gobechiya, J. A. Martens, A. Redl and B. F. Sels, *Green Chem.*, 2014, **16**, 695–707.
271 Y. Cao, J. Wang, M. Kang and Y. Zhu, *RSC Adv.*, 2015, **5**, 90904–90912.
272 Y. Cao, J. Wang, M. Kang and Y. Zhu, *J. Fuel Chem. Technol.*, 2016, **44**, 845–852.
273 C. Liu, C. Zhang, S. Hao, S. Sun, K. Liu, J. Xu, Y. Zhu and Y. Li, *Catal. Today*, 2016, **261**, 116–127.
274 H. Wang, C. Zhu, D. Li, Q. Liu, J. Tan, C. Wang, C. Cai and L. Ma, *Renew. Sustain. Energy Rev.*, 2019, **103**, 227–247.
275 S.-M. Wu, X.-Y. Yang and C. Janiak, *Angew. Chem., Int. Ed.*, 2019, **58**, 12340–12354.
276 H. Tabassum, A. Mahmood, B. Zhu, Z. Liang, R. Zhong, S. Guo and R. Zou, *Energy Environ. Sci.*, 2019, **12**, 2924–2956.
277 L. Liu and A. Corma, *Nat. Rev. Mater.*, 2021, **6**, 244–263.
278 H. Wang, L. Wang and F.-S. Xiao, *ACS Cent. Sci.*, 2020, **6**, 1685–1697.
279 X. Liu, Y. Liu, Y. Wu, S. Dong, G. Qi, C. Chen, S. Xi, P. Luo, Y. Dai, Y. Han, Y. Zhou, Y. Guo and J. Wang, *J. Hazard. Mater.*, 2023, **458**, 131848.
280 P. He, Q. Yi, H. Geng, Y. Shao, M. Liu, Z. Wu, W. Luo, Y. Liu and V. Valtchev, *ACS Catal.*, 2022, **12**, 14717–14726.
281 J. Xiao, K. Cheng, X. Xie, M. Wang, S. Xing, Y. Liu, T. Hartman, D. Fu, K. Bossers, M. A. van Huis, A. van Blaaderen, Y. Wang and B. M. Weckhuysen, *Nat. Mater.*, 2022, **21**, 572–579.

282 J. Li, T. Cai, Y. Feng, X. Liu, N. Wang and Q. Sun, *Sci. China Chem.*, 2024, **67**, 2911–2917.
283 K. Cheng, L. I. van der Wal, H. Yoshida, J. Oenema, J. Harmel, Z. Zhang, G. Sunley, J. Zečević and K. P. de Jong, *Angew. Chem., Int. Ed.*, 2020, **59**, 3592–3600.
284 C. Wang, L. Wang, J. Zhang, H. Wang, J. P. Lewis and F.-S. Xiao, *J. Am. Chem. Soc.*, 2016, **138**, 7880–7883.
285 Y. Chai, W. Shang, W. Li, G. Wu, W. Dai, N. Guan and L. Li, *Adv. Sci.*, 2019, **6**, 1900299.
286 Y. Wang, C. Wang, L. Wang, L. Wang and F.-S. Xiao, *Acc. Chem. Res.*, 2021, **54**, 2579–2590.
287 J. Zhang, L. Wang, B. Zhang, H. Zhao, U. Kolb, Y. Zhu, L. Liu, Y. Han, G. Wang, C. Wang, D. S. Su, B. C. Gates and F. S. Xiao, *Nat. Catal.*, 2018, **1**, 540–546.
288 W. Luo, M. Sankar, A. M. Beale, Q. He, C. J. Kiely, P. C. A. Bruijnincx and B. M. Weckhuysen, *Nat. Commun.*, 2015, **6**, 6540.
289 X. Pan, F. Jiao, D. Miao and X. Bao, *Chem. Rev.*, 2021, **121**, 6588–6609.
290 K. Cheng, L. C. J. Smulders, L. I. van der Wal, J. Oenema, J. D. Meeldijk, N. L. Visser, G. Sunley, T. Roberts, Z. Xu, E. Doskocil, H. Yoshida, Y. Zheng, J. Zecevic, P. E. de Jongh and K. P. de Jong, *Science*, 2022, **377**, 204–208.
291 Q. Zhang, S. Q. Gao and J. H. Yu, *Chem. Rev.*, 2023, **123**, 6039–6106.
292 Z. P. Hu, J. Han, Y. Wei and Z. Liu, *ACS Catal.*, 2022, **12**, 5060–5076.
293 J. He, Z. Wu, Q. Gu, Y. Liu, S. Chu, S. Chen, Y. Zhang, B. Yang, T. Chen, A. Wang, B. M. Weckhuysen, T. Zhang and W. Luo, *Angew. Chem., Int. Ed.*, 2021, **60**, 23713–23721.
294 H. J. Cho, D. Kim, S. Li, D. Su, D. Ma and B. J. Xu, *ACS Catal.*, 2020, **10**, 3340–3348.
295 IRENA, *Global Energy Transformation: A Roadmap to 2050*, International Renewable Energy Agency, 2018, http://refhub.elsevier.com/S2589-5974(19)30149-2/rf0005.
296 G. Xu, A. Wang, J. Pang, X. Zhao, J. Xu, N. Lei, J. Wang, M. Zheng, J. Yin and T. Zhang, *ChemSusChem*, 2017, **10**, 1390–1394.
297 C. Yang, Z. Miao, F. Zhang, L. Li, Y. Liu, A. Wang and T. Zhang, *Green Chem.*, 2018, **20**, 2142.
298 N. Olson, N. Deshpande, S. Gunduz, U. S. Ozkan and N. A. Brunelli, *Catal. Today*, 2019, **323**, 69–75.
299 L.-J. Liu, Z.-M. Wang, S. Fu, Z.-B. Si, Z. Huang, T.-H. Liu, H.-Q. Yang and C.-W. Hu, *Catal. Sci. Technol.*, 2021, **11**, 1537–1543.
300 Y. Román-Leshkov, M. Moliner, J. A. Labinger and M. E. Davis, *Angew. Chem., Int. Ed.*, 2010, **49**, 8954–8957.
301 V. Choudhary, S. H. Mushrif, C. Ho, A. Anderko, V. Nikolakis, N. S. Marinkovic, A. I. Frenkel, S. I. Sandler and D. G. Vlachos, *J. Am. Chem. Soc.*, 2013, **135**, 3997–4006.
302 C. Liu, C. Zhang, S. Sun, K. Liu, S. Hao, J. Xu, Y. Zhu and Y. Li, *ACS Catal.*, 2015, **5**, 4612–4623.
303 B. Zada, M. Chen, C. Chen, L. Yan, Q. Xu, W. Li, Q. Guo and Y. Fu, *Sci. China Chem.*, 2017, **60**, 853–869.
304 H. Li, H. Li and J.-F. Deng, *Catal. Today*, 2002, **74**, 53–63.
305 H. Li, W. Wang and J.-F. Deng, *J. Catal.*, 2000, **191**, 257–260.
306 P. Gallezot, P. J. Cerino, B. Blanc, G. Flèche and P. Fuertes, *J. Catal.*, 1994, **146**, 93–102.
307 B. W. Hoffer, E. Crezee, F. Devred, P. R. M. Mooijman, W. G. Sloof, P. J. Kooyman, A. D. van Langeveld, F. Kapteijn and J. A. Moulijn, *Appl. Catal., A*, 2003, **253**, 437–452.
308 J.-P. Mikkola, H. Vainio, T. Salmi, R. Sjöholm, T. Ollonqvist and J. Väyrynen, *Appl. Catal., A*, 2000, **196**, 143–155.
309 K. van Gorp, E. Boerman, C. V. Cavenaghi and P. H. Berben, *Catal. Today*, 1999, **52**, 349–361.
310 J. Wisnlak and R. Simon, *Ind. Eng. Chem. Prod. Res. Dev.*, 1979, **18**, 50–57.
311 T. Zhang, A. Q. Wang, M. M. Zheng, C. Li, J. Pang, T. N. Kalnes, J. Q. Chen, and J. A. Kocal, *US pat.* 08323937, 2012.
312 J. D. DeMartini, S. Pattathil, J. S. Miller, H. Li, M. G. Hahn and C. E. Wyman, *Energy Environ. Sci.*, 2013, **6**, 898–909.
313 J. Pang, M. Zheng, R. Sun, L. Song, A. Wang, X. Wang and T. Zhang, *Bioresour. Technol.*, 2015, **175**, 424–429.
314 T. D. J. te Molder, S. R. A. Kersten, J.-P. Lange and M. P. Ruiz, *Ind. Eng. Chem. Res.*, 2021, **60**, 13515–13522.
315 J. B. Powell and J. N. Chheda, *US pat.* US14/574661, 2014.
316 A. Yamaguchi, O. Sato, N. Mimura, Y. Hirosaki, H. Kobayashi, A. Fukuoka and M. Shirai, *Catal. Commun.*, 2014, **54**, 22–26.
317 K. Fabičovicová, M. Lucas and P. Claus, *ChemSusChem*, 2016, **9**, 2804–2815.
318 L. Shuai, M. T. Amiri, Y. M. Questell-Santiago, F. Heŕoguel, Y. Li, H. Kim, R. Meilan, C. Chapple, J. Ralph and J. S. Luterbacher, *Science*, 2016, **354**, 329–333.
319 B. Zong, X. Mu, X. Zhang, X. Meng and M. Qiao, *Chin. J. Catal.*, 2013, **34**, 828–837.
320 B. Xiao, M. Zheng, J. Pang, Y. Jiang, H. Wang, R. Sun, A. Wang, X. Wang and T. Zhang, *Ind. Eng. Chem. Res.*, 2015, **54**, 5862–5869.
321 https://www.dicp.ac.cn/xwdt/kyjz/202410/t20241017_7402288.html.
322 Y. Yang, D. Ren, Z. Ding, C. Shang, C. Li and S. Lee, *Mater. Today Sustain.*, 2024, **27**, 100838.
323 Y. Yang, Z. Ding, D. Ren, C. Shang, C. Li, F. Yang, B. Zhou, S. Hao, K. Sun and S. Lee, *Mater. Today Sustain.*, 2023, **24**, 100494.
324 W. Liu, Y. Chen, H. Qi, L. Zhang, W. Yan, X. Liu, X. Yang, S. Miao, W. Wang, C. Liu, A. Wang, J. Li and T. Zhang, *Angew. Chem., Int. Ed.*, 2018, **57**, 7071–7075.